Chapter 6
High Resolution Optical Coherence Tomography for Bio-Imaging

Jianhua Mo, Xiaojun Yu and Linbo Liu

Abstract Optical coherence tomography (OCT) is a low-coherence interferometry based bio-imaging technology. It has attracted extensive research interests in recent years for its non-invasive, high-speed and high-resolution properties. Numerous schemes for improving OCT resolutions have been demonstrated in literature. This chapter gives a comprehensive review of the recent developments of spectral domain (SD)-OCT systems with either high axial-resolution or lateral resolution, and then highlights the wide applications of such high-resolution OCT systems in biomedical imaging process. The influences of high-resolution OCT systems towards translational medicine are also discussed.

1 Introduction

Optical Coherence Tomography (OCT) is a powerful non-invasive imaging technique based on low coherence interferometry [1–3]. Through measuring the magnitude and echo time delay of the backscattered light, it is able to provide micrometer-scale cross-sectional images of biological tissues. Since its invention in early 1990s, OCT has attracted extensive research interests, and now has become a well-established clinical diagnostic routine for the detection of eye and skin diseases [4, 5].

J. Mo
School of Electronic and Information Engineering,
SooChow University, Soochow, People's Republic of China

X. Yu · L. Liu
School of Electrical and Electronic Engineering,
Nanyang Technological University, Nanyang, Singapore
e-mail: XJYu@ntu.edu.sg

L. Liu (✉)
School of Chemical and Biomedical Engineering,
Nanyang Technological University, Nanyang, Singapore
e-mail: liulinbo@ntu.edu.sg

M. Olivo and U. S. Dinish (eds.), *Frontiers in Biophotonics for Translational Medicine*, Progress in Optical Science and Photonics 3,
DOI 10.1007/978-981-287-627-0_6

OCT has several advantages over those commonly used conventional imaging modalities [2]. First, OCT imaging is non-invasive, non-ionizing, and thus safe for in vivo clinic applications; secondly, it is of very high speed, and can produce images nearly at video-rate; Lastly, OCT system can be constructed with small size and low cost fiber-optics, opening the possibility of miniature OCT system. More importantly, as the thickness of mucosa of luminal organs ranges from tens of microns to several millimeters, and many common lesions occur within the depth range of OCT imaging (2–3 mm), the potential clinical applications of OCT are particularly bright and exciting. OCT may fill the valuable niche in high resolution deep tissue imaging, owing to its micrometer-scale three-dimensional spatial resolution and high sensitivity.

High resolution OCT systems are highly desired for diagnostic purposes because cytological structures including cell type, cell shape, nuclear morphology, and mitotic activities can be visualized [6, 7]. These cellular morphological features together with extracellular structures are critical for accurate diagnosis of various diseases, such as cardiovascular diseases, eye diseases, cancers, and respiratory airway diseases. Currently, histopathologic analysis of biopsy tissues is the clinical gold standard for disease diagnosis. Note that histopathology relies on the examination of tissue samples at the cellular and subcellular resolution, which however is subject to sampling errors during tissue excision and processing artifacts and consequently may not reflect the pathophysiological processes in vivo. In addition, it is highly risky to excise tissues from some organs, such as coronary arteries. High resolution OCT can image cellular and extracellular structures in vivo quantitatively and noninvasively and thus can improve the diagnostic accuracy by eliminating the sampling error and artifacts mentioned above.

2 Fourier Domain OCT Principle

From late 1980 till now, OCT has been undergoing a rapid development, from time-domain (TD)-OCT to Fourier-domain (FD)-OCT, which has two forms, spectrometer-based/spectral domain OCT termed as SD-OCT and swept source based OCT termed as SS-OCT (also called optical frequency domain imaging (OFDI)). To date, FD-OCT has become the dominant form of OCT imaging system for its improved sensitivity and speed compared to TD-OCT [8]. This chapter will be focused on Fourier domain OCT. Most of Fourier domain OCT systems are developed based on Michelson interferometer as depicted in Fig. 1. The light photons emitted by the light source are split and delivered to the reference reflector and samples with multiple reflective surfaces (z_1, z_2, … z_n). Unlike TD-OCT, the reference reflector of FD-OCT is fixed. The photons reflected back by the reference reflector interfere with those scattered back from multiple reflective surfaces inside the sample, which is finally recorded by a detector as spectrum output to computer.

As mentioned above, FD-OCT has two forms, SD-OCT and OFDI. The differences between these two forms mainly lie in the light source and detector. In

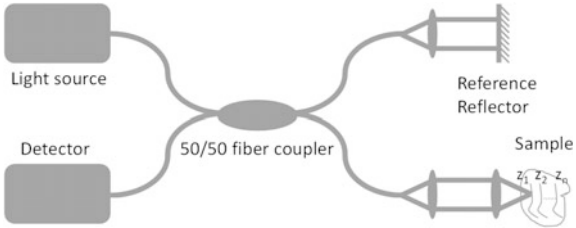

Fig. 1 Schematic of Michelson interferometer for FD-OCT

SD-OCT, superluminesent diode (SLD) is used as the light source, emitting the photons of the entire spectral range simultaneously. And a spectrometer is employed to resolve the interference signal in wavelength space and measure the full interference spectrum. OFDI uses wavelength-swept sources to replace SLDs, meaning that the photons at each frequency are output in sequence as a function of time. The interference signal are measured by a photo receiver rather than a spectrometer in a sequence of frequency as a function of time. In spite of the differences mentioned above, both SD-OCT and OFDI share the key math behind the theory. The measured interference spectrum in FD-OCT can be described with the following equation [9]:

$$I(k) = I_r(k) + 2\sqrt{I_s(k)I_r(k)}\sum_n \alpha_n \cos(k \cdot z_n) + I_s(k) \tag{1}$$

where $I_r(k)$ and $I_s(k)$ denote the intensities of the spectra reflected from the reference reflector and the sample, respectively, and k is referred to as the wavenumber. The interference between the reference signal and the signal from the sample is described by the second term of the right-hand side of the equation, where α_n represents the square root of the sample reflectivity at depth z_n. Finally, inverse Fourier transform of the measured interference spectrum gives the depth reflectivity profile of the sample as illustrated by the equation below [9]:

$$\left|FT^{-1}[I(k)]\right|^2 = \Gamma^2(z) \otimes \left\{\delta(0) + \sum_n \alpha_n^2 \delta(z - z_n) + \sum_n \alpha_n^2 \delta(z + z_n) + O\left[I_s^2/I_r^2\right]\right\} \tag{2}$$

where $\Gamma(z)$denotes the envelope of the coherence function of the laser source. On the right-hand side of the equation, the braces incorporate two different types of signals. One is the autocorrelation signals from the reference arm ($\delta(0)$) and the sample arm ($O[I_s^2/I_r^2]$), which are considered as noise in OCT. It is clearly seen that the autocorrelation signal from the reference arm is basically the DC part of the depth reflectivity profile with a fixed unity magnitude, while the autocorrelation signal from the sample is on the order of I_s^2/I_r^2, which can be reduced by increasing the power of the reference light. The other type of signal is the cross-correlation

signal (interference) between the reference arm and the sample. This is the signal, giving the insights into the depth reflectivity profile of the sample. It is worth noting that since the detector only measures the magnitude of the interference spectrum but no phase information, inverse Fourier transform generates two mirrored terms. Usually, one term is retained to create image. From the discussion above, a point measurement on sample surface can produce the depth profile of the sample at that particular location. Combined with the depth scanning by OCT, scanning the focused light beam in two lateral dimensions over the sample surface can produce a three-dimensional reflectivity structure image of the sample.

3 OCT Systems with High Axial Resolution

Axial resolution is an important parameter, linked to the performance of OCT, and is determined by the temporal coherence property of the OCT light source. It is usually defined as half of the coherence length of the light source [10, 11], i.e., the full-width at half-maximum (FWHM) of the light source self-coherence function (SCF) times light speed. SCF is the inverse Fourier transform of the source intensity spectrum. Under Gaussian approximation of spectrum distribution, axial resolution Δz of an OCT can be expressed below,

$$\Delta z = \frac{2\ln 2}{\pi} \times \frac{\lambda_c^2}{\Delta\lambda} \approx 0.44 \frac{\lambda_c^2}{\Delta\lambda} \tag{3}$$

where λ_c and $\Delta\lambda$ are the center wavelength and spectral bandwidth of the light source, respectively. Equation (3) indicates that axial resolution of OCT imaging can be improved by using the light sources with broader bandwidth and/or shorter central wavelength. Consider that biological tissue shows a decreased scattering cross-section with the longer wavelength and a strong absorption by water, haemoglobin and melanin in visible and near infrared range, which influence the light penetration depth and scattering structure contrast significantly. Therefore, wavelength selection of light sources is a compromise between axial resolution and penetration depth and scattering structure contrast. So far, the two major wavelength regions used for OCT are centered at 800 and 1300 nm. Assuming a Gaussian shape light source spectrum and a nondispersive imaging medium, the theoretical calculation of axial resolution Δz with respect to the light source optical bandwidth $\Delta\lambda$ shows that a light source with 180 nm bandwidth centered at 800 nm achieves an axial resolution of 1.6 μm, while with the 1300 nm light source, the resolution is around 4.1 μm.

3.1 High Resolution OCT System Development

3.1.1 OCT System Development with 800 nm Light Source

So far, most of the commercial time-domain (TD)-OCT systems from Carl Zeiss Meditec (Dublin, CA, USA) and Ophthalmic Technologies Incorporated (Toronto, ON, Canada) adopt super luminescent diodes (SLD) with an optical bandwidth of 20 nm centred at 820 nm. Spectral profiles of the light sources used in such systems are depicted in Fig. 2 [12], which allow for an axial resolution of 8–10 μm [13, 14]. For other types of lab-built TD-OCT systems with 800 nm region light sources, the reader is referred to reference [15].

Compared to TD-OCT, the second generation OCT technology, termed spectral domain OCT (SD-OCT), has the advantages of both increased imaging speed and increased signal to noise ratio (SNR) [16]. SD-OCT is initially built for high-speed in vivo ophthalmic imaging [17–22]. The highest axial resolution of such systems is around 6.2–14.4 μm using SLD with a central wavelength λ_c = 810–840 nm and FWHM bandwidth $\Delta\lambda$ = 20–50 nm. Various very high-speed SD-OCT and spectral-domain optical coherence microscopy (SD-OCM) systems were built. A line-field SD-OCT system for very high-speed three-dimensional (3D) retinal imaging was demonstrated in [23], while a compact ultrahigh-speed spectral-domain optical coherence microscopy (SD-OCM) was presented in [24]. More recently, a dual-band FD-OCT system with depth-related compensations was demonstrated to achieve an improved spectroscopic contrast and sensitivity [25]. Although resolutions of such systems are better than those of the conventional microscopy systems, they are still significantly below the technical limit and is

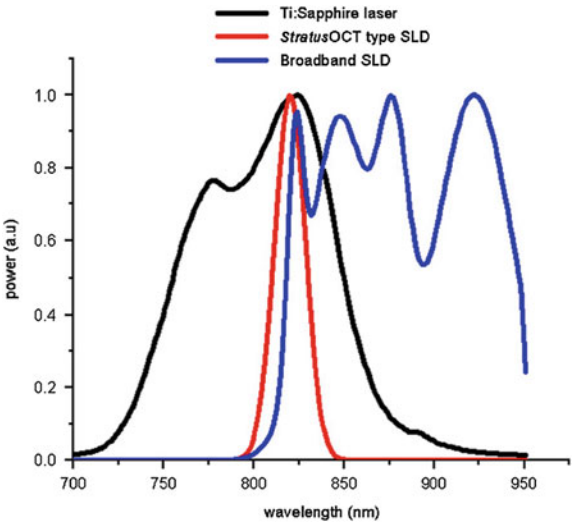

Fig. 2 Spectral bandwidth profiles of the light sources currently used in OCT imaging. (Figure is reproduced with permission from [12])

insufficient to identify individual cells or to assess subcellular structures such as nuclei or mitotic figures [15].

To view more details of the microstructures of the tissues, SD-OCT systems with ultrahigh axial resolutions at a-few-micrometer scale have been demonstrated [23, 24, 26–28]. The first ultrahigh-resolution OCT structural intensity images and movies of the human retina were reported in [26]. Figure 3a shows the schematic of the SD-OCT system that was used for imaging. The light source, which has a center wavelength $\lambda_c = 890$ nm and a FWHM bandwidth $\Delta\lambda = 150$ nm, was a combination of two SLDs with central wavelengths of approximately 840 and 920 nm,

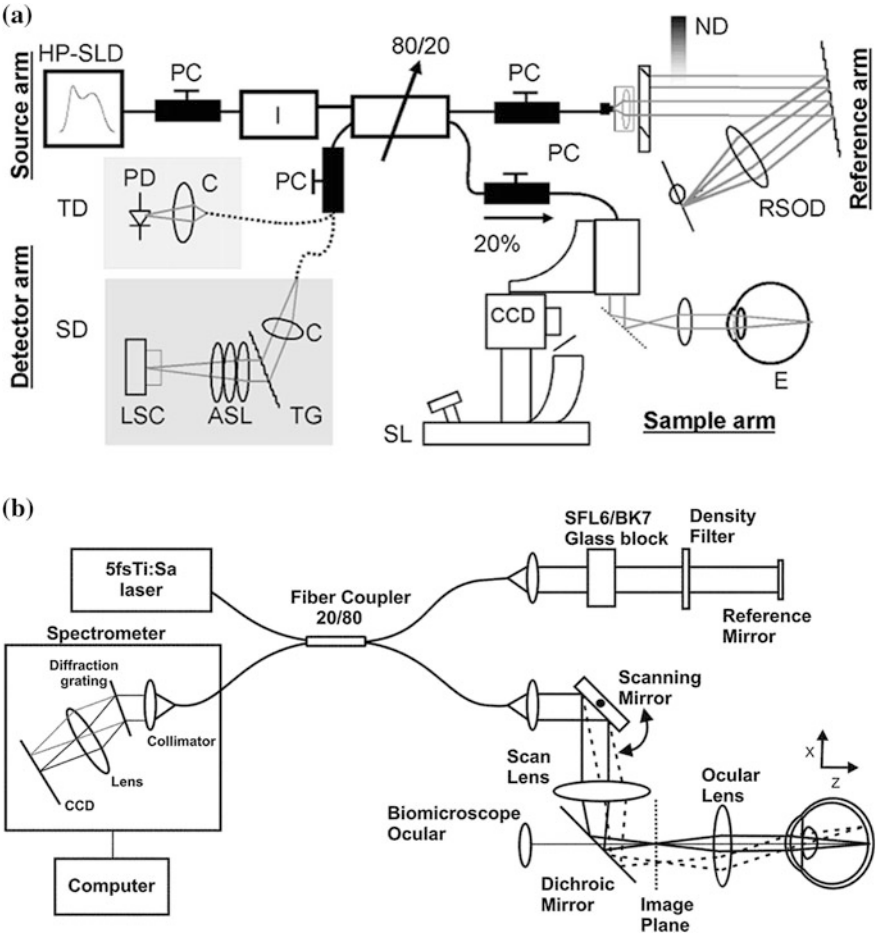

Fig. 3 OCT systems demonstrated using 800 nm light sources. **a** Schematic of the ultrahigh resolution SD-OCT system demonstrated in [18] using SLDs. **b** Schematic of the high-speed ultrahigh resolution SD-OCT system demonstrated in [27] using Ti:sapphire laser. (Figure is reproduced with permission from [18, 27])

respectively. Such a SD-OCT system is able to visualize the two layers at the location of the retinal pigmented epithelium as well as the small blood vessels in the inner and outer plexiform layers. The in vivo imaging speed reaches 29.3 frames per second with 500 A-lines per frame. The axial resolution was measured to be 4.0 μm in air from a mirror, and to be 3.5 μm from the specular reflection of the foveal umbo in vivo in a healthy human eye.

In addition to SLD light sources, broadband femtosecond Ti:sapphire lasers have also been commonly used to achieve high axial resolution in SD-OCT systems [27, 28]. Figure 3b presents the ultrahigh resolution SD-OCT system [27] using a 5 fs Ti:Sapphire laser source; the spectrum of the Ti:Sapphire laser source is measured to be ∼144 nm. The axial resolution was measured to be 2.1 μm in tissue. The high imaging speed together with the ultrahigh resolution of the system enables motion-free, high definition images. A similar femtosecond pulsed Ti:sapphire laser with a center wavelength of λ_c = 800 nm and a FWHM bandwidth $\Delta\lambda$ = 120 nm was also utilized in an ultrahigh resolution SD-OCT for high-speed in vivo imaging in [28]. The system adopted a 90:10 fiber coupler to realize the Michelson interferometric configuration, and achieved an axial resolution of ∼2.5 μm.

3.1.2 OCT System Development with 1300 nm Light Source

High sensitivity and long penetration depth are highly desired for OCT system to be used for imaging in vivo. Due to the wavelength-dependent scattering effect in tissue, it has been shown that optimal wavelength for longer imaging depth is around 1.3–1.5 μm [29]. High-speed high-sensitivity FD-OCT systems, with the form in SD-OCT or SS-OCT, were built using wavelengths in such region.

OCT systems implemented using 1.3 μm commercially available [5, 30–33] or custom-made [32, 34–37] frequency-swept laser sources have been demonstrated. A typical high-speed SS-OCT system was demonstrated in [30]. Through utilizing a frequency-swept laser with a center wavelength of λ_c = 1.32 μm and FWHM bandwidth around $\Delta\lambda$ = 60 nm, such system was able to achieve an imaging depth of 3.8 mm at an A-line acquisition rate of 15.7 kHz with a free-space axial resolution of 13.5 μm and a high sensitivity of −110 dB. Such a high-speed together with the high-sensitivity offers a significant potential in biomedical imaging, especially the in vivo applications, such as upper gastrointestinal tract imaging, intracoronary imaging and arterial structure imaging [31]. Figure 4 depicts the schematic of the demonstrated OCT system [30].

By detecting the frequency components of generated interferograms, SD-OCT systems using 1.3 μm laser sources have also been demonstrated [38–46]. Such SD-OCT systems were initially proposed for non-ophthalmic applications for its increased optical penetration within tissues at 1.3 μm and over 10-times higher imaging speed as compared to TD-OCT [38, 42]. In recent years, with the subsequent advances in broadband light sources, micrometer-scale ultrahigh-resolution imaging became possible and various software systems for real-time imaging display have also been developed [42, 44, 45]. The maximum scanning speed achieved

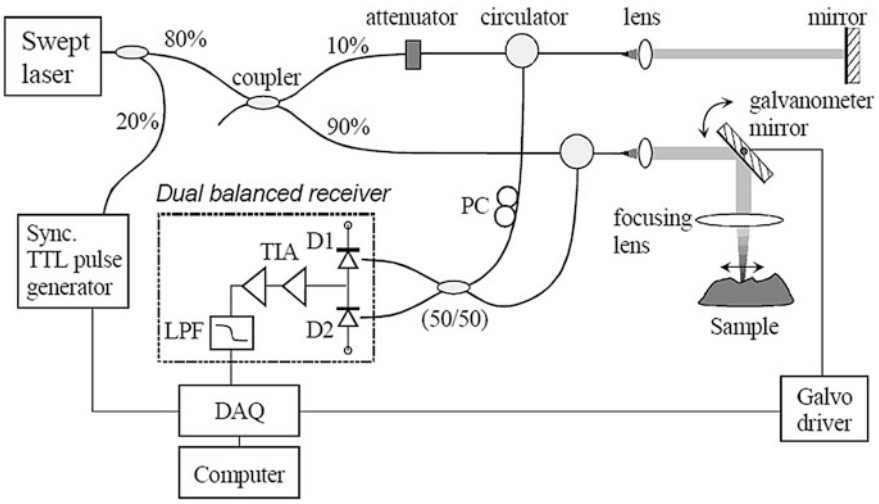

Fig. 4 SS-OCT system demonstrated using 1300 nm light source demonstrated in [30]. (Figures are reproduced with permission from [30])

by the SD-OCT systems reaches 38 frame per second (19,000 A-line per second) [38], and the real-time processing and display rate reaches 20 frames per second [44]. By far, SD-OCT systems using 1.3 μm light source have been successfully demonstrated to image normal and pathologic microarchitectures of skin, cardiovascular system, gastrointestinal tract, human thyroid gland, intestines, and cerebral edema, etc. [39–41, 43, 45, 46]. For endoscopic OCT imaging application, an axial resolution of 5 μm in air and 3.7 μm in tissue can be achieved by using the Cr^{4+}: Forsterite laser with center wavelength of 1.25 μm FWHM bandwidth of $\Delta\lambda = 210$ nm [40].

3.1.3 OCT System Development Using Other Types of Light Sources

A photonic crystal fiber in combination with a compact sub-10-fs Ti:sapphire laser was used for the first time as a light source for TD-OCT in [47]. Through proper selection of the input pulse parameters and PCF characteristics, a light source with FWHM bandwidth of $\Delta\lambda = 325$ nm centered at $\lambda_c = 725$ nm was achieved, which in turn produced an axial resolution of 0.75 μm in air (corresponding to 0.5 μm in biological tissue). Such ultrahigh resolution permits the in vitro visualization of human subcellular structures. With the water dispersion taken into account, results in [48] showed that the optimal wavelength region for OCT systems to eliminate the influence of depth-dependent water dispersion in tissue is centered at 1.0 μm. The first attempt to use 1.0 μm wavelength region light source for real-time OCT imaging was for a TD-OCT system [49]. An axial resolution of <4 μm in tissue was

achieved by using a compact femtosecond Nd:Glass laser that is spectrally broadened in a high numerical aperture single mode fiber.

OCT imaging at 800 nm wavelength region guarantees an ultrahigh resolution but image depth is limited, while the 1300 nm wavelength region generates enhanced image depth yet the axial resolution is not as high. To achieve a compromise between the image penetration depth and axial resolution, various frequency domain OCT systems using light sources with ~1000 nm center wavelength have been demonstrated. The two SS-OCT systems built in [50, 51] are of ultrahigh imaging speed. Specifically, the imaging speed of the former reaches 100–400 K axial scan per second, while the speed of the latter one is adjustable from 50 to 580 K per second.

OCT systems operate at center wavelength of 1050 nm is especially suitable for imaging the posterior segment due to the low-water-absorption window around 1050 nm. A 1.0 μm SD-OCT as an alternative to an ophthalmic 830 nm system was presented [52]. This system was able to achieve an axial resolution of 7.4 μm with ranging depth of 4.2 mm in tissue, and sensitivity of 98.5 dB at a speed of 38,300 axial scans per second. To further improve the penetration depth, another system using 1.05 μm was demonstrated in [53] to achieve an imaging depth of 6.1 mm in air. SD-OCT systems have also been widely applied for either ex vivo or in vivo biological tissue imaging in different cases, including intestines [41], retinal nerve fiber [54], human breast tissue [55], cataract patient posterior segment [52, 53, 56] and anterior segment [51], etc. Figure 5 depicts an ultrahigh-speed 1.0 μm SD-OCT system. The system has also been applied for in vivo retina imaging, and results

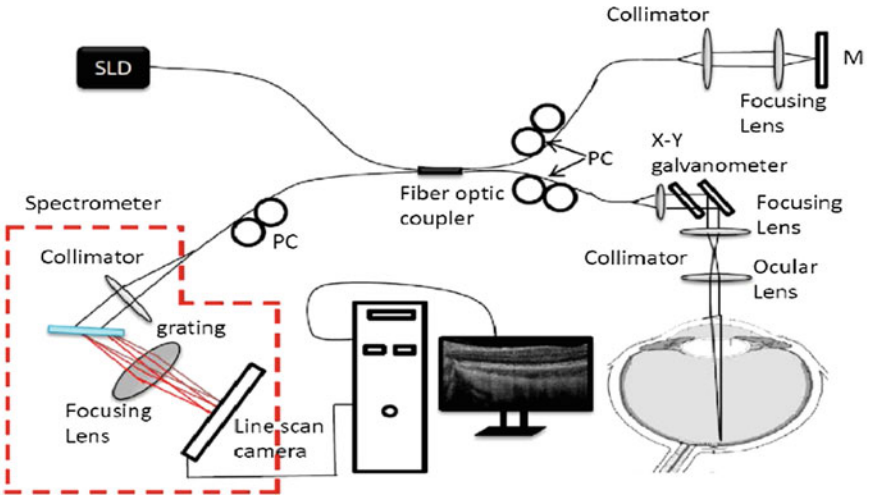

Fig. 5 A demonstrated 1.0 μm SD-OCT system [53]. (Figures are reproduced with permission from [53])

demonstrated that the proposed system is comparable to typical 1 μm SS-OCT system in providing a large field of the posterior segment of the human eye, and thus may motivate further investigations.

3.2 *High Resolution OCT Systems for Biological Imaging*

High resolution OCT systems have been widely utilized for various tissue imaging. Among such applications, the main one has focused on ocular disease analysis and characterization, especially for small animals, in the past years [15, 57–62]. An SD-OCT system with an axial image resolution of 2.8 μm was firstly used for in vivo, three-dimensional (3D) rat retina imaging in [57]. Figure 6 presents the imaging results from the rat retina [57]. Figure 6a demonstrates a 3D OCT volume rendering of the rat retina. The individual cross-sectional images acquired by the system, i.e., Fig. 6c, demonstrated an excellent visualization of fine retinal layers and a good correlation with the histology as shown in Fig. 6b. Application of high-resolution SD-OCT for 3D retinal imaging of small animals, as well as morphologic variations in outer retinal layers in human eyes were also reported in [60, 61], respectively. Detailed review on the developments of ultrabroad-bandwidth and tunable light sources, as well as high-speed Fourier detection techniques for retinal imaging applications can be found in [15, 58, 59].

In addition to ophthalmic imaging, high resolution OCT systems have also been tested as an optical biopsy tool in neurosurgery for ex vivo and in vitro brain tissue imaging for small animals [63, 64]. With two broadband light sources, i.e., a prismless Ti:sapphire (λ_c = 800 nm, $\Delta\lambda$ = 260 nm) laser and a fiber-based (λ_c = 1350 nm, $\Delta\lambda$ = 470 nm) laser, interfaced alternatively for imaging, a sub-2 μm axial resolution in biological tissue was achieved. Images on the scale from single neuron cells to the structural organization of entire small-animal brain [63], as well

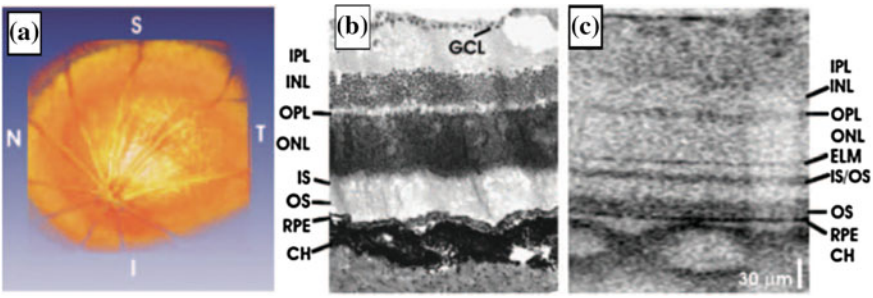

Fig. 6 In vivo rat retina images acquired by a high-speed, high-resolution SD-OCT system [57]. The high speed system acquired 24,000 axial scans per second enables the generation of the in vivo 3D volumetric renderings of the retina (**a**). The individual cross-sectional images (**c**) acquired by such system compared well with histology (**b**) in visualizing the many fine layers of the retina. (Figures are reproduced with permission from [57])

as for both healthy and pathological human brain tissues [64] were captured as shown in Fig. 7. Figure 7a presents the tomograms of the honeybee brain, while Fig. 7b, c shows the tomograms of the healthy human brain tissue and that with ganglioglioma, respectively. This study suggests that high-resolution OCT systems could find applications as an investigative tool in basic neurological research, even though technological advancements are still required to improve the diagnostics capabilities for real-time, non-invasive in vivo biopsy in neurosurgery.

High-resolution OCT systems with 800 nm region light sources have been utilized for internal organs imaging in different cases. Since endoscopy requires probes to be positioned in the vicinity of the respective surfaces for imaging, several miniaturized catheter imaging probes for endoscopic OCT systems have been presented [65, 66]. A multimodality system that combines both OCT and laser-induced fluorescence (LIF) in a 2.0-mm-diameter endoscopic package was described in [67] for mouse colon imaging. Later, probes using reference reflection originating from the inside surface of the glass envelope at the distal end of the endoscope for in vivo mouse colon imaging was demonstrated in [65, 66]. Figure 8a presents an endoscopy probe that was proposed for mouse colon imaging in vivo. Comparison between the endoscopic OCT tomograms (Fig. 8b, c) and stained histologic cross-section image (Fig. 8d) demonstrated that the microscopic features that are too small to be visualized in mouse tissue with conventional

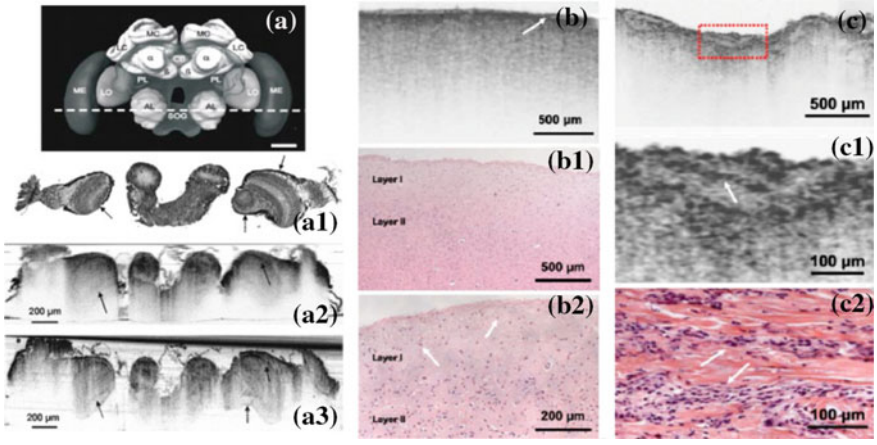

Fig. 7 OCT systems for both ex vivo and in vitro brain tissue morphology imaging in neurosurgery [63, 64]. **a** Schematic representation of the honeybee brain. The comparison between stained cross-section histology (**a1**) and OCT images acquired at a resolution of 3 × 1.4 µm (lateral × axial) with 110-dB sensitivity (**a2**), and resolution of 4.5 × 1.4 µm (lateral × axial) with 98-dB sensitivity (**a3**), respectively. **b** OCT tomogram of healthy brain tissue acquired with resolution of 0.9 × 2 µm (axial × lateral) compared to representative H&E-stained histological sections (**b1–b2**). **c** OCT tomogram (2 × 1 mm) of ganglioglioma; **c1** an enlarged view of the region marked with *red dotted line* in (**c**), compared to the corresponding H&E-stained histological section (**c2**). (Figures are reproduced with permission from [63, 64])

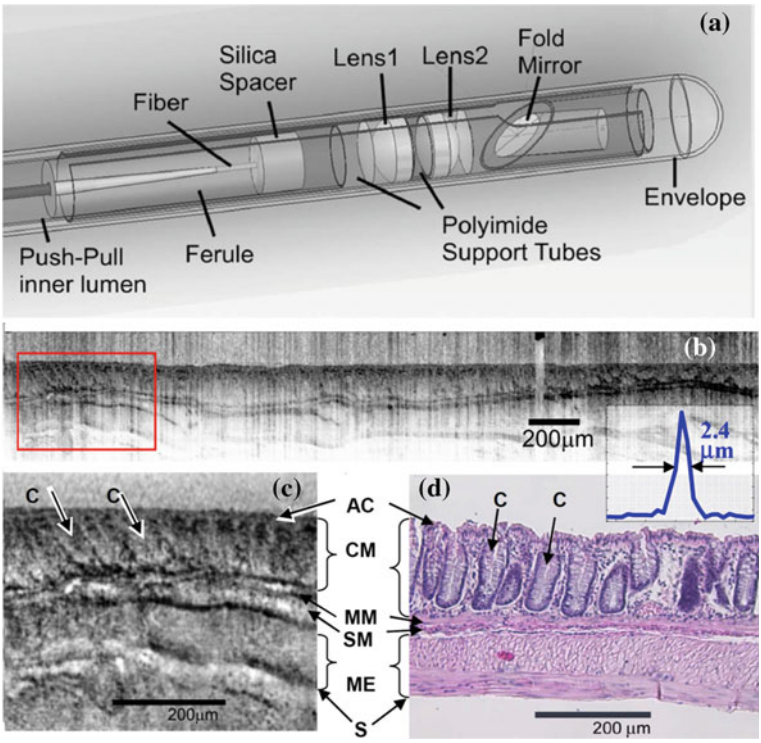

Fig. 8 High-resolution endoscopy OCT for in vivo mouse colon imaging [65, 66]. **a** An endoscopic OCT probe model for colon imaging. The acquired endoscopic OCT tomograms (**b** and **c**) compared to the stained histologic cross-section image. Endoscopic OCT enables visualization of colonic mucosa (CM), muscular mucosa (MM), submucosa (SM), muscularis externa (ME), and serosa (S) layers. Contrast enhanced portion, using local histogram equalization shows a surface layer of apical crypt cells (AC) as well as vertical structures in the mucosa that may correspond to crypt boundaries (**c**) [65]. (Figures are reproduced with permission from [65, 66])

resolution systems, including colonic crypts, now can be clearly resolved using the proposed OCT system [65, 66].

OCT system using 1.3 μm light sources has large potential in biomedical imaging, especially the in vivo applications, such as upper gastrointestinal tract imaging, intracoronary imaging and arterial structure imaging [31]. The SS-OCT system demonstrated in [30] was utilized for clinic imaging of different biological tissues. Figure 9 demonstrate the in vivo images [31] of coronary artery, porcine esophagus, porcine coronary artery and porcine coronary artery, respectively, acquired by the system. The OCT system built in [5] was for demonstrating the stability, portability and reproducibility of a set of automated algorithms that are specially developed for analyzing three-dimensional OCT volumetric imaging of human skin. Some more compact custom made source-swept laser sources have

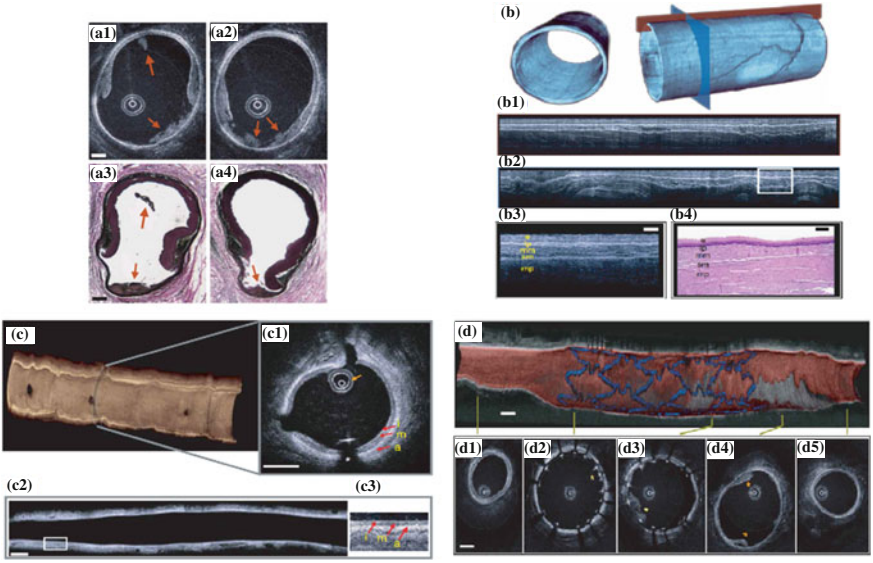

Fig. 9 The clinic applications of the 1.3 μm OFDI system for esophageal mucosa and of coronary arteries in vivo imaging [31]. **a** Cross-sectional images of dissected coronary artery and its comparison to histology. **b–b4** Porcine esophagus in vivo. **c–c3** Porcine coronary artery in vivo. **d–d5** Stented porcine coronary artery in vivo. (Figures are reproduced with permission from [30, 31])

also been developed and adopted for OCT systems. A custom-made all-fiber laser consisting of semiconductor optical amplifier (SOA) and Fabry-Perot tunable filter (FFP-TF) formed in a ring cavity was adopted to build an OCT system in [37].

4 OCT Systems with High-Lateral Resolution

Lateral resolution is another critical factor that governs the performance of an OCT system. OCT lateral resolution is solely determined by the diffraction limited spot size of the focused beam, and is defined as the $1/e^2$ beam waist of a Gaussian beam. According to the definition, this spot size is inversely proportional to the numerical aperture of the objective beam. Previous analysis has depicted the relationship between lateral resolution and axial field view for OCT system in Fig. 10 [2]. If a Gaussian input beam is assumed, the transverse resolution Δx can be defined by

$$\Delta x = \frac{2\lambda}{\pi}\frac{1}{\mathrm{NA}} = \frac{4\lambda}{\pi}\frac{\mathrm{f}}{\mathrm{d}} \tag{4}$$

where $NA = d/2f$ is the numerical aperture of the objective lens, with f being the focal length of the objective lens and d being the diameter of the beam entering the

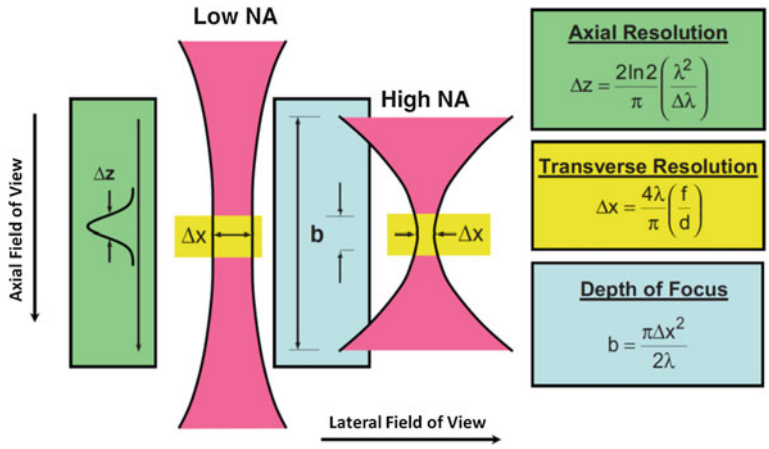

Fig. 10 Schematic of OCT sample arm optics [2]. The low and high numerical aperture (NA) optics geometries show a trade-off between lateral resolution and depth of focus for an OCT system. (Figures are reproduced with permission from [2])

objective. With the same assumption, the depth of focus (DOF), defined by the confocal parameter b, which is twice the Rayleigh length z_R, can be expressed as below,

$$b = 2z_R = \frac{\pi \Delta x^2 \lambda}{\lambda}. \tag{5}$$

The above definitions show an inevitable trade-off between the lateral resolution and DOF for an OCT system: increasing numerical aperture of the focusing system improves the lateral resolution by reducing the focal spot size, yet it decreases the DOF. To achieve a high lateral resolution along with an extended DOF, various approaches have been proposed. Those methods can be classified into three categories, i.e., adaptive optics/digital-refocusing, axicon optics and phase/amplitude apodization.

4.1 Methods for High-Lateral Resolution OCT Systems

4.1.1 Adaptive Optics/Digital-Refocusing

Digital refocusing methods have been receiving great research efforts for extending the focal-depth of OCT imaging since it requires no or very subtle hardware modifications on conventional FD-OCT. Consequently, various digital refocusing methods have been reported in the past decade. One of the early reported digital refocusing methods is interferometric synthetic aperture microscopy (ISAM) [68].

In principle, this method retrieves the spatially invariant sharp focus at out-of-focus planes/depths through solving the inverse problem of light scattering and diffraction. The mechanism of synthetic aperture concept underlying the inverse problem is that when the focused light beam is scanned over the sample surface laterally, the scattering component can be considered as being illuminated by different optical apertures at each OCT measurement (A-scan) no matter whether the scattering component is in-focus or out-of-focus. This assumption is valid based on the fact that the scattering component only overlaps with part of the light spot and moreover the light beam is focused so that different parts of the light spot have different incident angles. The measured OCT signal can be expressed as a function of the light beam's transverse coordinate r_0 and the wavenumber k as shown by equation below [68],

$$S(r_0,k) = \mathrm{A}(k) \int_{\Sigma} d^2 r \int_{V} d^3 r' G(r', r, k) g(r' - r_0, k) \times \eta(r') g(r - r_0, k) \qquad (6)$$

where A(k) denotes the power spectral density of the light source. g and G are the normalized Gaussian beam profile and the Green function, respectively. $\eta(r')$ represents the scattering potential. By taking two-dimensional Fourier transform of Eq. (6) and other derivations, the three-dimensional Fourier transform of the scattering potential of the sample can be related to the two-dimensional Fourier transform of the measured interference signal as illustrated by Eq. (7).

$$\tilde{S}(Q,k) = A(k)\left(\frac{i2\pi^2}{k_z(Q/2)}\frac{k^2}{\alpha^2}\exp\left(-\frac{\alpha^2 Q^2}{4k^2}\right)\right)\tilde{\tilde{\eta}}(Q; -2k_z(Q/2)) \qquad (7)$$

where Q is the transverse wave vector, k_z is the axial component of the wave vector and $\alpha = \pi/NA$ (NA is the numerical aperture of the objective). $\tilde{S}(Q,k)$ denotes the two-dimensional Fourier transform of $S(r_0, k)$ with respect to r_0, and $\tilde{\tilde{\eta}}(Q; -2k_z(Q/2))$ is generated from one-dimension Fourier transform of $\tilde{\eta}(Q; z)$ (two-dimensional transverse Fourier transform of the scattering potential $\eta(r')$ in Eq. (6)) with respect to z. Finally, the 3D scattering structure image with spatially invariant resolution can be produced by solving the equation for the solution of the scattering potential.

Figure 11 demonstrates the efficacy of ISAM method with images of artificial phantom with embedded titanium dioxide. The system used for OCT measurement is configured with an objective (focal length = 12 mm, NA = 0.05), which leads to a 5.6 μm focal spot size and a confocal parameter of 239 μm. With the 6 en-face images (defocused slices 1–3 by conventional SD-OCT vs slices 4–6 by ISAM) in Fig. 11a, it is clearly seen that ISAM improved the focus significantly. The volumetric images (Fig. 11b, c) proves that ISAM works over the full image depth.

More recently, Mo et al. came up with a different novel digital refocusing method, called depth-encoded synthetic aperture method, exhibiting advantages like low computation cost, no requirement on phase stability and compatibility with

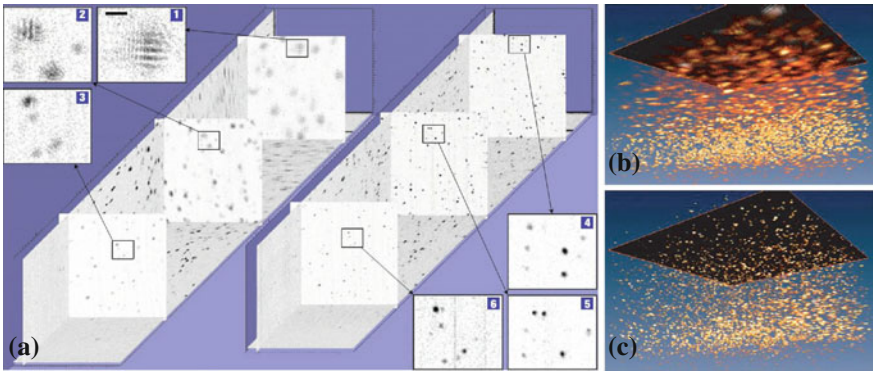

Fig. 11 **a** Orthoslice view of the conventional SD-OCT image and ISAM image of an artificial phantom with titanium dioxide as scatters. **b** and **c** are the corresponding volumetric view. *En-face* images *1–3* for conventional SD-OCT and *4–6* for ISAM are 1100, 475 and −240 μm away from the focal plane, the *minus sign* indicates that the plane below the focal plane. (Figures are reproduced with permission from [68])

most of common OCT configurations [69]. Briefly, this method retrieves or improves the focus by correcting the curvature of the collected light wavefront resulting from the defocus effect. The principle of this method is illustrated in detail in Fig. 12. To explain the method, the wavefront of the scattered field is analyzed. An annular phase plate (3-mm thick polycarbonate plate with a circular hole at the center) is inserted into the sample arm at the back focal plane of the imaging lens. The phase plate segments the scattered light into approximately two equal parts, central beam through the central hole and edge beam through the polycarbonate plate. When the scatter is in-focus, the collected light travels through the phase plate with a planar wavefront (Fig. 12a). The edge beam is delayed with respect to the central beam due to the longer optical path length introduced by the phase plate, Δz $(n - 1)$ (Δz is the thickness of the phase plate, and n is the refractive index of the phase plate). In a single OCT B-scan, this delay encodes the two images formed by those two beams to different depths with a separation of $\Delta z(n - 1)$. This allows for reconstructing a new image by coherently adding those two images via correcting the delay due to the phase plate (Fig. 12b). The new image can have a comparable lateral resolution as the image acquired without the phase plate. In comparison, when the scatter is out-of-focus, for example above the focal depth (Fig. 12c), the wavefront of the collected light field is curved due to the defocus effect. This adds a small extra delay (δz) to the edge beam in addition to the delay $\Delta z(n - 1)$ caused by the phase plate as discussed above. This small extra delay is also discussed in another work on self-interference fluorescence microscopy (SIFM) [70]. Similar to the in-focus situation, a new image with improved focus can be reconstructed by correcting the edge beam wavefront for both the terms $\Delta z(n - 1)$ and δz (Fig. 12d).

In real OCT implementation, with a phase plate inserted into the sample arm, three different paths are created for the sample arm light to reach the detector via a

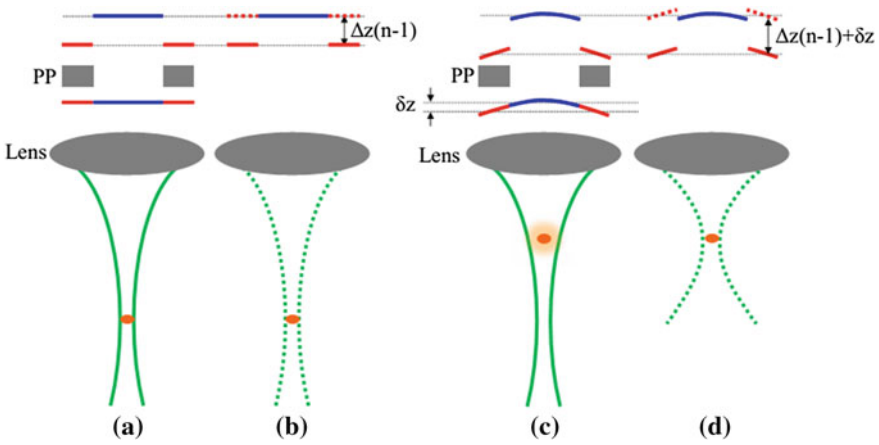

Fig. 12 Illustration of the principle of the depth-encoded synthetic aperture method for extending the depth-of-focus of optical coherence tomography. The drawing shows the source of the scattered light (*orange dot*), the lens, the beam diameter as a function of the axial position defined by Gaussian optics (*solid green*), the reconstructed beam diameter after image processing (*dotted green*), the wavefronts before and after the phase plate (*blue* and *red lines*) in (**a**) and (**c**). Δz and n are the thickness and refractive index of the annular phase plate (PP). (Figures are reproduced with permission from [69])

scattering object in the sample, which are defined as three optical apertures: (1) optical aperture 1, the light path passes through the center of the phase plate both on the way to the scattering object and back; (2) optical aperture 2, the light path passes through the center on the way to the scattering object and travels back through the edge, or, equivalently, passes through the edge on the way to the scattering object and travels back through the center; (3) optical aperture 3, the light path passes through the edge of the phase plate both on the way to the scattering object and back.

Mathematically, the measured interference signal via the three optical apertures above can be expressed by the following equations:

$$\begin{aligned} I(k) = \sqrt{I_r(k)I_s(k)}\alpha\{&[\exp(i2kz)\mathrm{K} \\ &+ \exp(i2kz + ik(\Delta z(n-1) + \delta z))\mathrm{K} \\ &+ \exp(i2kz + ik2(\Delta z(n-1) + \delta z))] + C.C.\} \end{aligned} \tag{8}$$

where $\Delta z(n-1)$ and δz (it is zero for in-focus case) have been defined above, C.C. indicates the complex conjugate. The first, middle and third terms in the closed brackets on the right of the equation represent the images formed by optical aperture 1, 2 and 3, respectively, which are also called top image, middle image and bottom image in single OCT B-scan. To facilitate the image processing of summing coherently the three terms (three images), by rewriting k as $k = k_0 + \Delta k$, the second

and third terms are simplified as illustrated by the following Eqs. (9) and (10), respectively:

$$I(k) = \exp(i\psi_{middle})\sqrt{I_r(k)I_s(k)}\alpha \exp(i2kz)\exp(i\Delta k\Delta z(n-1)) + C.C.$$
$$\text{with } \psi_{middle} = k_0\Delta z(n-1) + k_0\delta z \tag{9}$$

$$I(k) = \exp(i\psi_{bottom})\sqrt{I_r(k)I_s(k)}\alpha \exp(i2kz)\exp(i2\Delta k\Delta z(n-1)) + C.C.$$
$$\text{with } \psi_{bottom} = 2k_0\Delta z(n-1) + 2k_0\delta z \tag{10}$$

compared to the OCT signal detected without phase plate, an extra oscillation phase ($\Delta k\Delta z(n-1)$) and a constant phase ψ are added in Eqs. (9) and (10), resulting from the phase plate and defocus effect. The phase term ($k_0\delta z$) is negative when the focal plane is below the imaging target and positive when the focal plane is above the imaging target. In theory, the focus can be recovered by correcting the defocus-induced $k_0\delta z$ in the detected OCT signal. This is used as the theoretical basis for digital refocusing process to be discussed in the following part. The digital refocusing processing includes two steps: (1) the first step is to depth-decode the middle and bottom images to the depth position of the top image to correct the depth-offset due to the phase plate ($\Delta z(n-1)$); (2) the second step is to correct the defocus-induced additional phase change ψ. This phase change is wavenumber-independent and therefore can be corrected simply by applying a constant phase factor to the Fourier-transformed spectrum which undergoes a frequency-shift in the first step. Then, all three complex images are coherently summed to reconstruct a new image. The images with two beads as an example in the colored windows in Fig. 13 provide detailed insight into the reconstruction process and how the focus is improved. The phase manipulation leads to constructive interference on the center

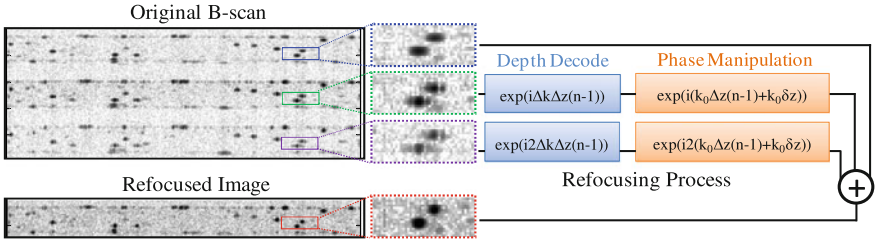

Fig. 13 Refocusing process: a single B-scan contains three images of the same object at different depths (i.e., *top*, *middle* and *bottom*); the first step is to correct the depth-separation due to the phase plate for the *middle* and *bottom* images (*blue text box*). Then, the phase of the *middle* and *bottom* images are further manipulated (*orange text box*) and coherently added to the *top* image to construct a new image with improved lateral resolution. The four colored windows are zoomed-in images of two beads to better visualize the refocusing process. The image is 1.28 mm wide and its aspect ratio is 3:1. (Figures are reproduced with permission from [69])

part of the focus spot and destructive interference on the edge part of the focus spot (i.e., side lobe in middle and bottom images). This combined constructive and deconstructive interference process improves the lateral resolution.

Figure 14 compares the digitally refocused images (panel III) with the conventional Gaussian beam images (panel I) and the truncated Gaussian beam image by optical aperture 1 (panel II). The sample used is a 300-μm thick artificial phantom created by embedding 5-μm melamine spheres into a silicone polymer. The subfigures (Fig. 14a–h) represent the images of the phantom being moved away from the objective at 80-μm step size, leading to a 115.2-μm displacement of the focal plane. From Fig. 14a–h, it is seen that the spheres in the truncated beam images appeared to have a very slow change in width over the defocus process. This can be explained by the fact that the light beam is truncated from 3.4 to 1.8 mm (diameter) by the phase plate which results in an extension of Rayleigh range at the cost of an increased lateral focal spot size. In contrast, the corresponding full beam image without phase plate experienced a much more rapid change in the sphere's width during the same defocus process. For the refocused images, it is obvious that as compared to the full beam image, the refocused image had comparable focus size and maintained the focus over a much larger depth range.

The efficacy of this digital refocusing method is further quantified by analyzing the full width at half maximum (FWHM) of the lateral intensity profiles of five spheres marked with red circle in Fig. 14d. The results show that the broadening of the spheres can be slowed down by approximately a factor of five in digitally refocused images as compared to the full Gaussian beam images. In addition, it is also found that this digital refocusing method appears to only suffer from a −1.9 to −4.1 dB energy efficiency loss as compared to the full beam imaging for in-focus situation, implying that this method is much more efficient than the depth-of-focus extension by phase-apodization or axicon lens illumination [71, 72].

Besides the two digital refocusing methods discussed above, there also exist other digital refocusing methods, such as deconvolution and scalar diffraction model. For deconvolution method, Yasuno et al. designed a depth-dependent complex deconvolution filter, which is used to manipulate the spatial frequency components of OCT image so as to improve the focus at out-of-focus depth range [73]. This phase doconvolution filter is originally developed from the Fourier-transform of the transverse point spread function of OCT image and further simplified into the following form:

$$H(\xi) = \exp\left(i\pi \frac{\lambda z_0}{2} \xi^2\right) \tag{11}$$

where z_0 is the depth distance from the actual focal plane, $\xi = x/\lambda f$ (x: the lateral position; λ: the light wavelength; f: the focal length of the objective). The deconvolution process basically comprises three steps: (1) Calculate discrete Fourier transform (DFT) of the complex OCT image for each lateral line; (2) Multiple the DFT of each lateral line with the designed deconvolution filter; (3) Calculate

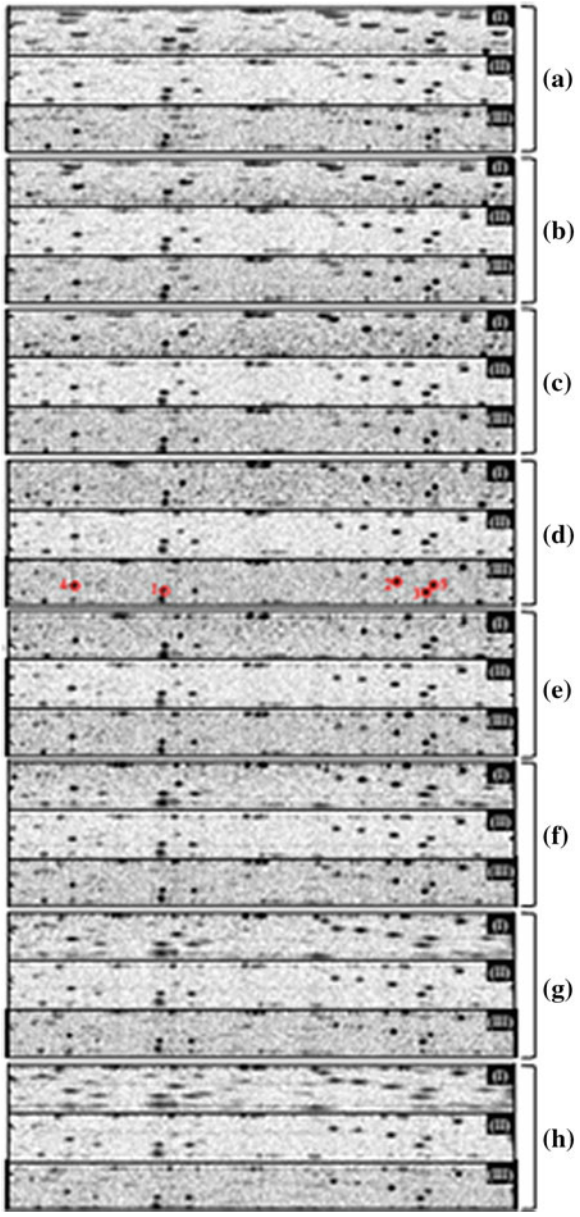

Fig. 14 **a–h** Intensity images acquired when the phantom is moved away from the objective at a physical step size of 80 μm. Each subfigure includes three imaging modes: full beam image (*top*), truncated Gaussian beam image (*middle*) and refocused image (*bottom*). All the images are presented on a logarithmic scale with the colormap clipped to 75 % of the maximum intensity of the image. The image is 1.28 mm wide and its aspect ratio is 3:1. (Figures are reproduced with permission from [69])

inverse DFT for each line to reconstruct a new OCT 3D volume image with an improved focus. This method was validated on razor blade and human eye. The results demonstrated that this method can improve not only the focus which is twice better than transform-limited resolution but also the signal-to-noise ratio. This method is non-iterative and consequently is not computationally expensive. Several

years later, an iterative deconvolution method was reported by Liu et al. [74]. This method utilizes the lateral PSF definition of OCT developed from Gaussian optics model as illustrated by the equation [75]: $h(x, y) = \exp\left(-2(x^2 + y^2)/w_z^2\right)$ where w_z is the depth-dependent focused beam spot size. Richardson-Lucy deconvolution method was employed to deconvolute the enface image at each depth with the lateral PSF. Thus, improving the image sharpness or correcting the defocus effect is equivalent to searching for the optimal lateral PSF, which further translates into optimal depth-dependent focused beam spot size w_z. To obtain the optimal focused beam spot size, the image evaluation function based on Information entropy was calculated for a predefined set of beam spot sizes and the discontinuity of the evaluation function determines the optimal focused beam spot size. This method is iterative and requires more computation time, and however it eliminates the need to measure the optical parameters of the OCT system.

For digital refocusing based on scalar diffraction model, Yu et al. reported to refocus the en-face images at defocused depths by back-propagating the light to the actual focal plane using two-dimensional scalar diffraction model [76]. Specifically, each complex en-face image produced from common OCT signal process is converted into angular spectrum by Fourier-transform. Then the light field was propagated for a distance z using angular spectrum method to cancel out the defocus effect. Finally, inverse Fourier-transform was calculated on the new angular spectrum to recover the en-face image with improved lateral focus. The optimal propagation distance z for each depth can be obtained from prior knowledge about the OCT system. Alternatively, a more time-consuming way is exhaustive search with image sharpness as criteria. Liu et al. proposed to use information entropy as the gold criteria to search for the optimal propagation distance z [77]. Both of the two methods described above were only demonstrated on low-scattering tissue, i.e., onion, and tissue with simple structure, i.e., fat, and was not applied to real biological tissues with complex scattering structures.

4.1.2 Axicon Optics

Axicon is an optical element that generates a narrow focal line along the optical axis [78]. Such a focal line can be approximated by a zero-order Bessel-type (nondiffracting) beam that preserves its transverse distribution along the axial axis, rendering a very large (compared with Rayleigh range) DOF [79]. Owing to this property, an axicon is usually combined with a spherical lens to produce a ring pattern in the focal plane of the lens, and is applied in OCT imaging system to achieve both high lateral resolution and large DOF simultaneously.

The first application of axicon lens to an OCT imaging system is the TD-OCT demonstrated by Ding et al. in [80]. Through utilizing an axicon lens with a top angle of 160° in front of the sample, a Bessel beam field distribution in the focal plane was generated. The results showed that a lateral resolution of 10 μm or better was achieved over a focusing depth of at least 6 mm; the focusing beam intensity

was approximately constant over the depth range. However, in such configuration, the central lobe of the generated Bessel field carries only 5 % of the total power, which seriously limits its applications for biomedical samples. Such a power loss becomes even worse when the detection beam passes through the axicon lens again in the reverse direction [72]. Both simulation and experimental results demonstrated that an axicon based OCT system suffers from a signal loss of ~13 dB at the peak for both illumination and detection beams compared with the conventional lens system [81]. The power loss effects are clearly shown in Fig. 15. More recent results demonstrate that the power efficiency of an axicon based system is solely dependent on the Fresnel number [82], and N-fold DOF gain may result in N-fold loss of the peak irradiance of the Bessel beam. In addition to the power loss issue, sidelobe artifacts were also introduced since more than 90 % optical power was distributed to higher order diffractions. The sidelobe artifacts significantly degraded the image quality especially in log scale images.

To address the power-loss issue of axicon-optics, one of the reported methods is to decouple the detection and illumination beams for the OCT system. Specifically, to extend DOF with Bessel beam illumination while enhance the scattering contrast, a dark-field illumination scheme was proposed for frequency domain optical coherence microscopy (FDOCM) in [72, 83, 84]. Figure 16 shows the proposed dark-field illumination scheme of the FDOCM system as well as the performance results obtained [72]. Experimental results demonstrated that a ten-fold DOF gain was achieved at a lateral resolution of 1.5 μm. Such scheme improves the power efficiency of the axicon lens based system and suppresses the sidelobes simultaneously, especially for the second and higher order sidelobes.

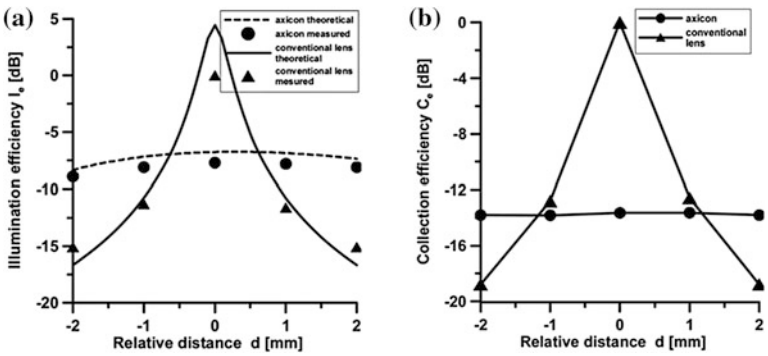

Fig. 15 The measured OCT illumination and detection efficiencies over focal range parameter *d* using axicon lens [81]. **a** The measured illumination efficiency versus *d*, **b** the measured detection efficiency versus *d*. (Figures are reproduced with permission from [81])

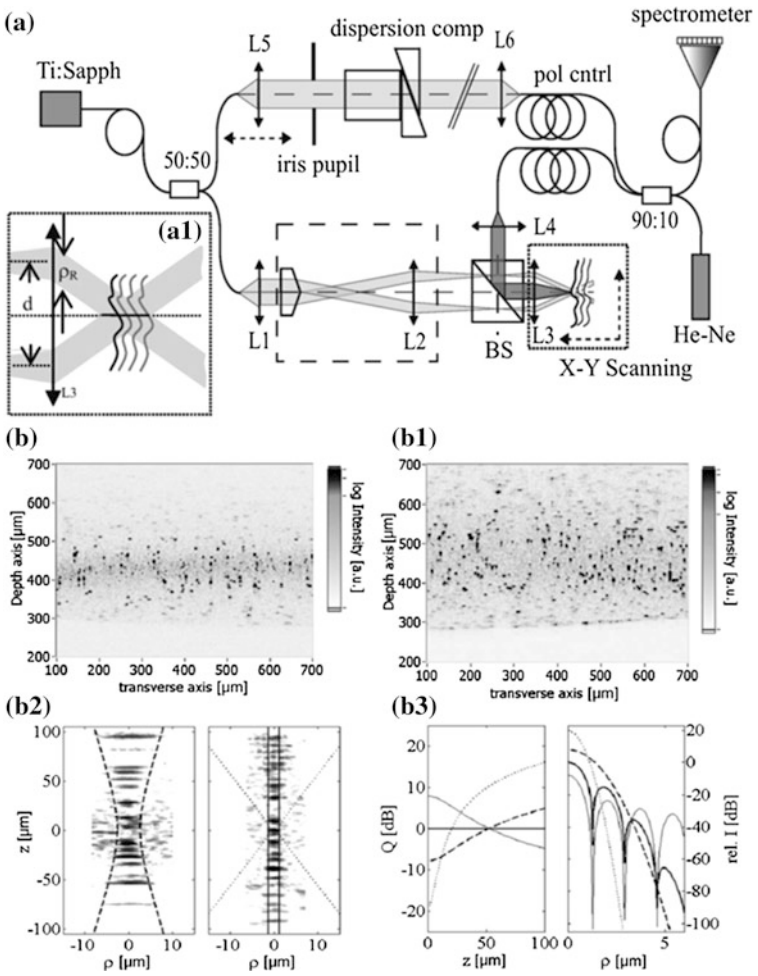

Fig. 16 A dark-field illumination scheme proposed for frequency-domain optical coherence microscopy (FDOCM) [72]. **a**–**a1** Schematic of the extend-field (xf) FDOCM. **b**–**b3** Measured results for FDOCM performance. (Figures are reproduced with permission from [72])

4.1.3 Phase/Amplitude Apodization

Compared to the bulk-optics axicon lens, phase/amplitude apodization based DOF extension scheme has attracted much attention in recent years since its fabrication and miniaturization are relatively easy [69]. Below we present a general principle for phase/amplitude apodization method to be used in OCT system.

Assume an SD-OCT setup (Fig. 17a) with two general pupil filters, which can be implemented using either phase or amplitude apodization method, adopted in reference and sample arm, respectively. The coordinates and notations around the

sample and focal planes are shown in Fig. 17b, c; assume a collimated input beam and an infinity-corrected objective lens, the normalized wavelength dependent field amplitude distribution around the focal region can be expressed as [86],

$$g(\mathrm{k},\rho,\mathrm{u}) = 2\sqrt{S(\mathrm{k})}\int_0^1 r\tilde{f}(\mathrm{k},\mathrm{r})J_0(\rho\mathrm{r})\exp\left[-\frac{1}{2}\mathrm{iur}^2\right]\mathrm{dr} \tag{12}$$

where $\mathrm{k} = 2\pi/\lambda$ is the wave number and λ is the wavelength of light source; r is the radial coordinate normalized by the radius a_0 of the filter 1 shown in Fig. 17b; ρ and u denote the simplified radial and axial coordinates in the sample space respectively, and are expressed as

$$\rho = k(\mathrm{NA})R, \tag{13}$$

$$u = k(\mathrm{NA})^2 Z, \tag{14}$$

with R and Z being the real radial and axial coordinates in the sample space, NA is the effective numerical aperture of the objective lens. $S(\mathrm{k})$ is the spectral intensity distribution of the light source; J_0 is a Bessel function of the first kind and order zero; $\tilde{f}(\mathrm{k},\mathrm{r})$ is the amplitude profile of the fiber mode in the pupil plane.

To generate an extended illumination focus, a general pupil filter $p_1(\mathrm{k}, \mathrm{r})$ as shown in Fig. 17b can be placed in the illumination arm. For such generalized phase/amplitude filter, its pupil function can be expressed as,

$$F_1(\mathrm{k},\mathrm{r}_1) = A_1(\mathrm{k},\mathrm{r}_1)\mathrm{P}_1(\mathrm{k},\mathrm{r}_1) \tag{15}$$

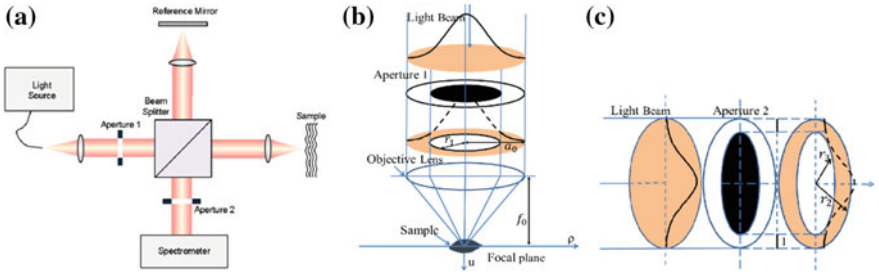

Fig. 17 **a** Schematic of a typical SD-OCT system with filter 1 adopted in the illumination path while filter 2 in the detection; **b** a collimated illumination light passes through the filter 1 and is focused by an infinity-corrected objective lens; **c** a detection light beam passes through the filter 2. (Figures are reproduced with permission from [85])

where $A_1(\mathrm{k}, \mathrm{r}_1)$ and $\mathrm{P}_1(\mathrm{k}, \mathrm{r}_1)$ are the expressions of amplitude and phase changes brought by pupil filter 1, respectively.

The process of a collimated illumination light (with radius a_0) passing through filter 1 and being focused onto the sample is shown in Fig. 17b. Under the condition of Gaussian approximation for circular, linear-polarized input light beam, the field distribution $\tilde{f}(\mathrm{k}, \mathrm{r})$ on the sample plane can be expressed as

$$\tilde{f}(\mathrm{k}, \mathrm{r}) = F_1(\mathrm{k}, \mathrm{r}_1) 2\pi [r_0(\mathrm{k})]^2 \exp\left\{ -\frac{1}{2} \left[\frac{2\pi r r_0(\mathrm{k}) a_0}{f_0 \lambda_c} \right]^2 \right\} \tag{16}$$

where f_0 is the focal length of the objective lens; λ_c is the center wavelength of the light source; r_1 is the obscuration radius of filter 1. $r_0(\mathrm{k})$ is the wavelength dependent fiber mode field radius. Under Gaussian approximation, such radius can be expressed as [87],

$$r_0(\mathrm{k}) = \frac{r_{co}}{\sqrt{2 \ln V(\mathrm{k})}} \tag{17}$$

where $V(\mathrm{k}) = \mathrm{k} r_{co} NA_f$ is the fiber parameter with NA_f being the effective fiber numerical aperture; r_{co} is the core radius of the single mode fiber, which is usually within the range of 2–5 μm.

In order to enhance the imaging system detection efficiency, another general type pupil filter 2, as shown in Fig. 17c, can be placed onto the detection arm. With the radii r_2 and r_3 that can be optimized for different purpose, this pupil filter $p_2(\mathrm{k}, \mathrm{r})$ can be expressed as,

$$F_2(\mathrm{k}, \mathrm{r}_2, \mathrm{r}_3) = A_2(\mathrm{k}, \mathrm{r}_2, \mathrm{r}_3)\, \mathrm{P}_2(\mathrm{k}, \mathrm{r}_2, \mathrm{r}_3) \tag{18}$$

With Gaussian approximation of circular, linear-polarized detection beam, the normalized wavelength dependent detection beam field amplitude distribution in the focal range can be expressed as,

$$\begin{aligned} g_{eff}(\rho, \mathrm{u}) &= \int_{k_{\min}}^{k_{\max}} [g(\mathrm{k}, \rho, \mathrm{u})]^2 F_1(\mathrm{k}, \mathrm{r}_1) F_2(\mathrm{k}, \mathrm{r}_2, \mathrm{r}_3) dk \\ &= \int_{k_{\min}}^{k_{\max}} [g(\mathrm{k}, \rho, \mathrm{u})]^2 A_1(\mathrm{k}, \mathrm{r}_1) P_1(\mathrm{k}, \mathrm{r}_1) A_2(\mathrm{k}, \mathrm{r}_2, \mathrm{r}_3) P_2(\mathrm{k}, \mathrm{r}_2, \mathrm{r}_3) dk \end{aligned} \tag{19}$$

where $k_{\min}$ and $k_{\max}$ are cut-off wave numbers.

Equation (19) shows that the light field distribution at the focal region is dependent on the radii of the general type filters $F_1(\mathrm{k}, \mathrm{r}_1)$ and $F_2(\mathrm{k}, \mathrm{r}_2, \mathrm{r}_3)$. With appropriate radii chosen for the pupil filters, both DOF extension and other objectives can be achieved simultaneously.

Phase-Masking Scheme

By far, various phase [88–90] or amplitude [91, 92] apodization schemes have been proposed for DOF extension of microscopy systems in literature. Phase mask is the easiest and most popular scheme for DOF extension. A four zone binary-phase spatial filter (BPSF), as shown in Fig. 18a, was proposed to engineer point-spread function of the optical coherence microscopy system in [71]. The radii of the zones are a, b, c, and 1. The phase of each zone Ø is set to be 0 or π with respect to the center wavelength λ_c. Such a BPSF was mapped to the pupil plane of the objective lens, as shown in Fig. 18b, with the modulated pupil filter functions being $F_1(k, r_1) = \exp[i\Phi(k, r_1)]$ and $F_2(k, r_2, r_3) = 1$, respectively. The effects of different radius values on the optimized PSFs are shown in Fig. 18c. Figure 18d shows the modulus of the effective axial PSFs of the confocal system and the systems

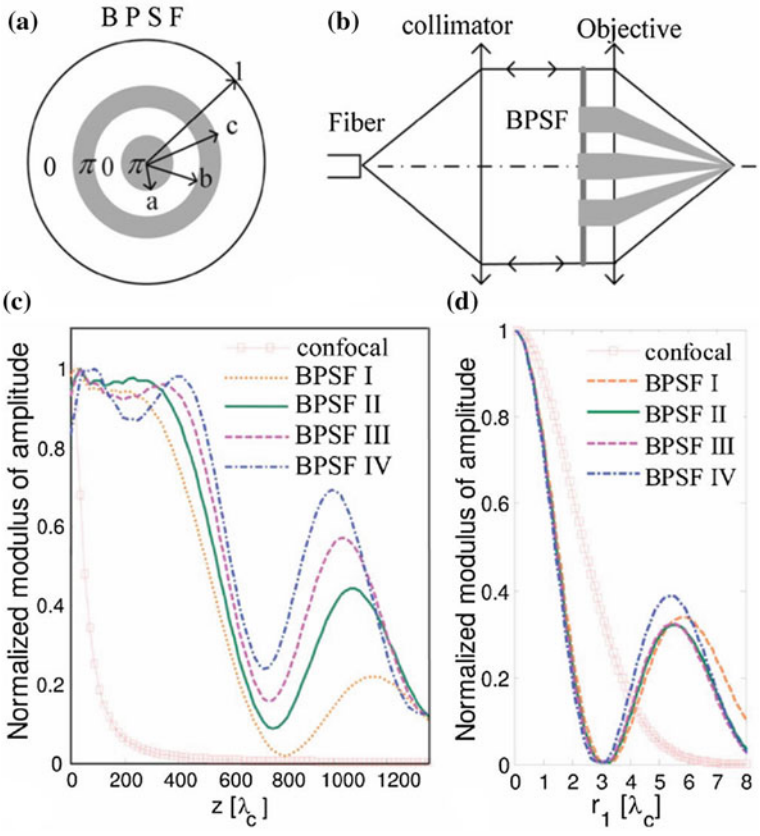

Fig. 18 **a** Schematic of the proposed BPSF filter; **b** BPSF optimized sample arm optics; **c** modulus of the axial beam profile; **d** modulus of the transverse beam profile in the focal plane. (Figures are reproduced with permission from [71])

optimized with different BPSFs. With the optimized radii, BPSF improved the center lobe power up to 28 % that of the total power defined by the $1/e^2$ beam waist, and a DOF gain of 10.5 was achieved with a lateral resolution of 5.0 μm.

Another phase-masking scheme in the regime of low Fresnel numbers was proposed for an ultrathin fiber probe [89]. Such phase mask consists of a short section of overfilled gradedindex (GRIN) fiber, and can be sliced in series with the distal focusing optics without any additional fabrication process. The beam propagation method based numerical simulation results show that a DOF gain of 1.55 can be obtained compared to the conventional lensed fiber probe with a lateral resolution of 7 μm. The more recent phase-masking scheme using either axially-symmetric filter [90] or seven-zone pupil filter [93] further demonstrated the effectiveness and potential of phase apodization scheme in extending DOF. Results show that a DOF gain of 30 can even be achieved with higher lateral resolution.

Amplitude-Apodization Schemes

Amplitude apodization has also been used in microscopy systems [92, 94, 95]. With an amplitude apodization filter, which can be expressed as below, a class of high-resolution OCT systems featured with 1–2 μm spatial resolution has been demonstrated. They were termed as Micro-OCT [92, 94–96], and were depicted as shown in Fig. 19a,

$$F_1(\mathrm{k}, \mathrm{r}_1) = \begin{cases} 1 & r_a > r_1 \\ 0 & otherwise \end{cases} \tag{20}$$

The μOCT system is a SD-OCT implementation with several key improvements to standard OCT that yield high resolution in both lateral and axial directions. The general layout and axial resolution characterizations are shown in Fig. 19a, b,

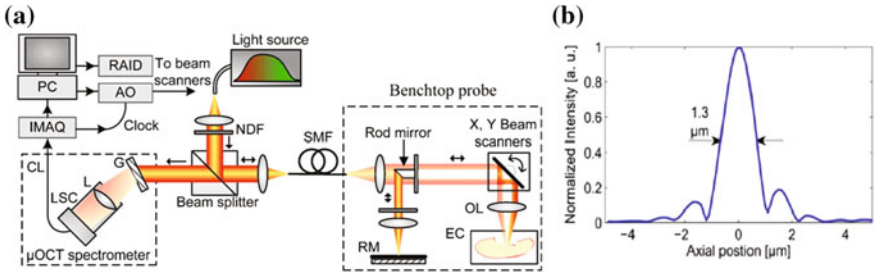

Fig. 19 μOCT instrumentation schematic and axial resolution [94]. **a** System diagram of the proposed μOCT system. **b** Depth profile of mirror surface, indicating an axial FWHM of 1.3 μm. (Figures are reproduced with permission from [94])

respectively. A super-continuum source (Fianium SC450) provides the high-bandwidth, short coherence length light necessary for high axial resolution (1.3 μm, Fig. 19b). A typical μOCT system includes an interferometer with the reference and sample arms intersecting at a beam-splitter. The beam-splitter is replaced in μOCT with a 45° rod mirror, which apodizes the sample beam by introducing a circular obscuration in the center to achieve a balance of good lateral resolution (2 μm) and long depth of focus (0.2 mm). Custom software is employed to control the galvanometer scanning motors while acquiring spectral data from the line camera. The system operates with user-configurable line and frame rates and customizable scan geometry; typical settings are 32 or 40 frames per second, 512 A-lines per frame in a linear scan, and 0.5 mm by 0.5 mm (X by Z) for a cross-sectional image. The effective thickness of each cross-section is equal to the μOCT beam spot size (2 μm).

More recently, research has been carried out to adopt center-obscured pupil filters at illumination and detection arms to achieve both extended depth of focus and sidelobe suppression for spectral-domain OCT system [85], wherein the pupil filter 1 and filter 2 are described as follows,

$$F_1(\mathrm{k}, \mathrm{r}_1) = \begin{cases} 1 & r_a > r_1 \\ 0 & otherwise \end{cases} \tag{21}$$

$$F_2(\mathrm{k}, \mathrm{r}_2, \mathrm{r}_3) = \begin{cases} 1 & r_2 < r_a < r_3 \\ 0 & otherwise \end{cases} \tag{22}$$

As shown in Eq. (19), the principle can be understood: when the center-obscured pupil filter 1 is adopted in the illumination arm, a quasi-Bessel illumination beam is generated. Although such quasi-Bessel beam helps generate a much larger DOF compared with the conventional focusing schemes [82], large sidelobes, which are only ~15 dB lower than the mainlobe, are introduced simultaneously [72]. Similarly, the pupil filter 2 adopted in the detection arm also introduces sidelobes to the sample arm optics. If the first sidelobe of the illumination PSF co-locates with the first minimum of the detection PSF, then the first sidelobe of the sample arm PSF will be largely suppressed. In this way, both DOF extension and first sidelobe suppression can be achieved simultaneously for an OCT system.

To demonstrate the advantages of the proposed technique, simulations are carried out to compare among different focusing systems: (1) a full aperture scheme with no pupil filter adopted (FA-OCT, Fig. 20a); (2) an annular aperture scheme with pupil filter 1 in both illumination and detection path (BF-OCT, Fig. 20b); (3) an annular aperture scheme with filter 2 in both illumination and detection path (Fig. 20c); (4) an annular aperture scheme with filter 1 in the illumination path and filter 2 in the detection path (DF-OCT, Fig. 20d). Simulation results shown in Fig. 20 demonstrate that a DOF gain of 4.2 can be achieved compared with the FA-OCT system of equal lateral resolution (Fig. 20a).

For the sidelobes introduced, it is shown that the normalized sidelobes are pronounced in the annular aperture schemes with the first sidelobe of −9.3 dB

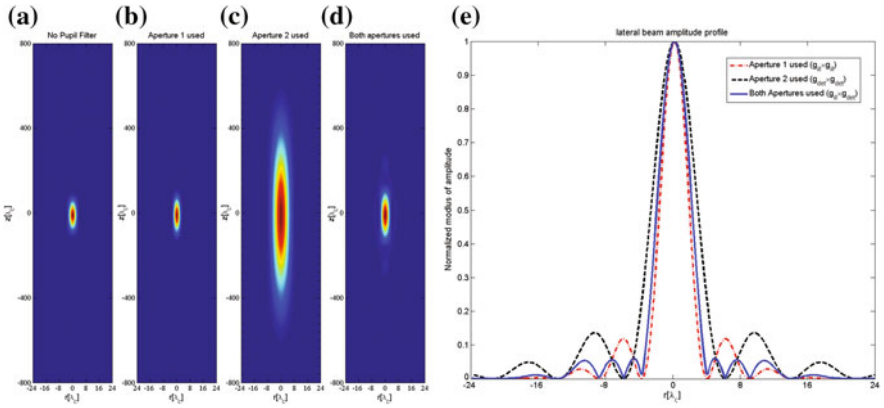

Fig. 20 Normalized intensity distributions in focal region of (**a**): a OCT system with no filter adopted, **b** OCT system with aperture 1 in both illumination and detection paths, **c** OCT system with aperture 2 in both illumination and detection paths, and **d** OCT system with filter 1 and filter 2 in illumination and detection path, respectively. **e** sidelobe suppression effect for the OCT system with filter 1 and filter 2 in illumination and detection path, respectively. (Figures are reproduced with permission from [85])

(Fig. 20b), and −8.7 dB (Fig. 20c), respectively, while with the two proposed pupil filters adopted (Fig. 20d), the sidelobes of all orders are below −12.2 dB (Fig. 20d) due to a first sidelobe suppression ratio of 2.9 and 3.5 dB, respectively. The sidelobe suppression effect by using a combination of the two pupil filters is further demonstrated in lateral profiles (Fig. 20e).

To further verify the theoretical predictions, a dark-field OCT (DF-OCT) system as shown in Fig. 21 was constructed. A superluminescent diode array (Superlum Broadlighters D-810-HP) with a center wavelength at 810 nm and a FWHM bandwidth of 100 nm was employed as the light source of the DF-OCT system. The output power was 8.62 mW. The generated light was collimated by a lens L1 (Cat# 378-823-5, M Plan APO 10×, Mitutoyo Inc.) first, and then was split by a 45º rod mirror RM1 (#54-092, Φ = 2 mm, Edmund Optics Inc.) with the circular portion at the center directed to the reference arm while the remaining annular portion to the sample arm. The annular beam coupled to the sample arm was again cropped by an aperture stop (diameter Φ = 5 mm), and then center-obscured by another 45º rod mirror RM2 (#54-094, Φ = 3 mm, Edmund Optics Inc.) before it was directed to a pair of galvo scanners (GVSM002/M, Thorlabs Inc.) and an objective lens L4 (AC127-025-B-ML, Thorlabs Inc.). The light power on the sample was around 1.31 mW.

The beam directed to the reference arm firstly passed through a 4-f system consisting of lens L2 and L3 (AC127-025-B-ML, Thorlabs Inc.) to balance the dispersion caused by the objective lens. It was then guided to a third rod mirror RM3 (#54-092, Φ = 2 mm, Edmund Optics Inc.) to combine with the signal beam backscattered from the sample. Finally, the combined beam was focused by a lens

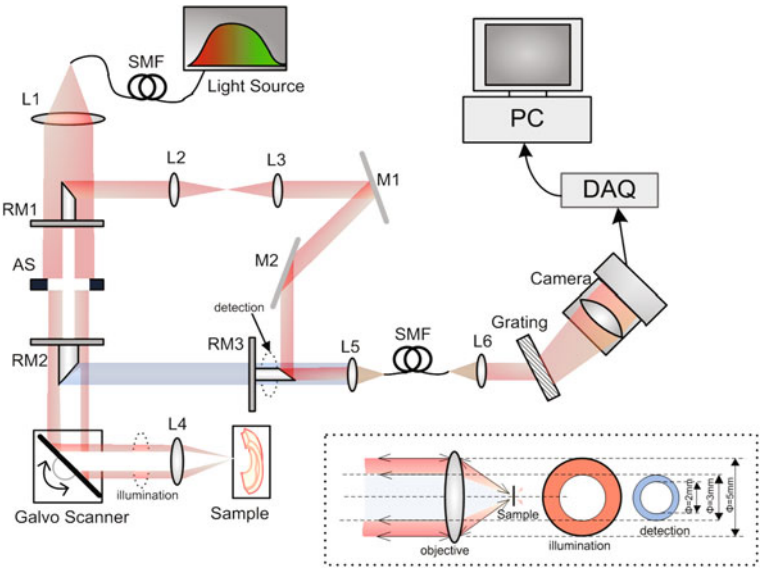

Fig. 21 Experimental configuration of the constructed DF-OCT imaging system. *L1–L6* lens. *RM1–RM3* rod mirror. *M1–M2* mirror. *AS* aperture stop. *SMF* single-mode-fiber. **a** The geometries of the dark-field illumination beam, illumination and detection pupil filters. (Figures are reproduced with permission from [85])

L5 (Cat# 378-823-5, M Plan APO 10×, Mitutoyo Inc.) into a single mode fiber (780-HP, Nufern) to the spectrometer. In the constructed DF-OCT system, the aperture stop AS together with rod mirror RM2 acted as the illumination pupil filter, while the rod mirrors RM2 and RM3 together acted as the detection pupil filter. The shapes and the radii of these two filters were shown in Fig. 21a.

The spectrometer consisted of a diffraction grating (1200 l/mm @ 830 nm, Wasatch Photonics Inc.), a camera lens (Nikon AF Nikkor 85 mm f/1.8D), and a line scan camera (E2V, AViiVA EM4). The detected signal was digitized at 12-bit digital resolution, and then was transferred to a computer through camera link cables and an image acquisition card (KBN-PCE-CL4-F, Bitflow Inc.). In the experiments, the camera and the galvo scanners were synchronized by a triggering signal generated by the computer. The effective camera pixel number was 868. The spectrometer efficiency, including the grating diffraction efficiency, sensor quantum efficiency, and camera lens efficiency, was measured to be 0.376. The line rate and the exposure time of the camera were set to be 10 kHz and 97.7 μs, respectively. The experimental axial and lateral resolutions of the DF-OCT system were measured to be 3.3 and 4.1 μm respectively, which match well with their corresponding theoretical values of 2.9 and 3.9 μm.

To assess the performance of the constructed DF-OCT system, a full aperture OCT (FA-OCT) system and a bright field OCT (BF-OCT) system with filter 1 in both illumination and detection arms were constructed for comparison. The light

source, spectrometer settings, illumination beam diameter, and objective lens were the same for these three systems.

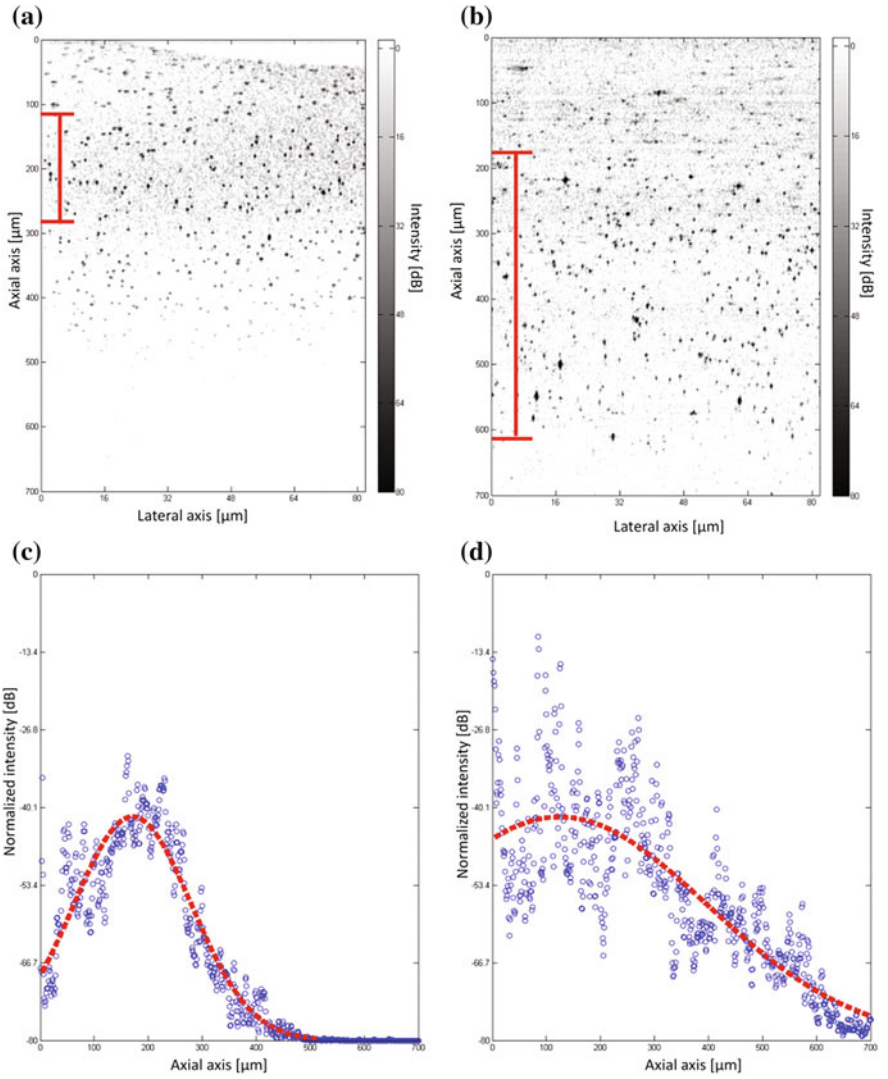

Fig. 22 Real-time tomograms of 800 nm latex calibration beads acquired with the FA-COT and the DF-OCT systems, respectively. Cross-sectional images of the microbeads acrose solution are grabbed with **a** FA-OCT system and **b** DF-OCT system. *Red bars* in the images indicate the DOF. The axial scatter plots of the normalized intensity of mircobeads scatterings are shown in **c** for FA-OCT system and **d** for DF-OCT system. The *dashed red curves* are Gaussian-fits of the assumed on-axis irradiance profiles to a subset of the microbeads cloud comprising only the strongest signals. (Figures are reproduced with permission from [85])

To demonstrate the DOF extension, an agarose solution (Cat# PC0701-500G, Vivantis Inc., ~0.5 %) of polystyrene microbeads (Cat# SIGMA/LB8-2ML, SIGMA Inc., Dia. 800 nm, ~0.1 vol.%) was used to characterize the focusing performances. Figure 22a, b present the cross-sectional images acquired using the FA-OCT and the DF-OCT systems, respectively, with capturing rate of 20 frames

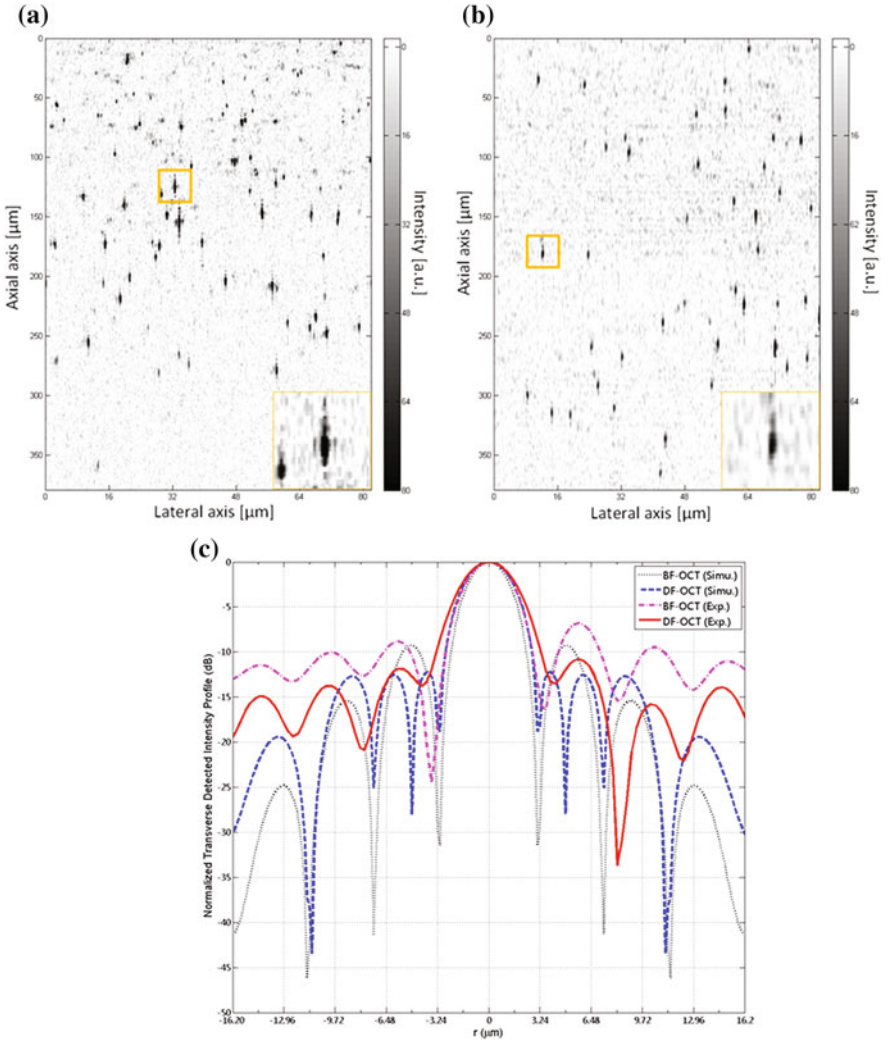

Fig. 23 Sidelobe suppression with the constructed dark-filed OCT (DF-OCT) system compared with that of the constructed bright field OCT (BF-OCT) system. Real-time tomograph of 800 nm microbeads are acquired with **a** BF-OCT system and **b** DF-OCT system. **c** Lateral intensity profiles of microbead images that are acquired using BF-OCT and DF-OCT setups, and are compared to the simulation results. (Figures are reproduced with permission from [85])

per second (fps). Each image covers a range of 82 μm × 775 μm with 393 lateral × 744 axial pixels (Width × Depth). The axial scatter plots of the normalized intensity of a large number of mircobeads scatterings for the two systems were plotted in Fig. 22c, d, respectively. The dashed red curves show Gaussian-fits of the assumed on-axis irradiance profiles to a subset of the microbeads cloud comprising only the strongest signals. Results demonstrate that the proposed DF-OCT system increased the DOF by factors of ∼3 and 1.1 compared with the FA-OCT and BF-OCT systems respectively.

To test the sidelobe suppression effect of the constructed DF-OCT system, the microbeads solution again was used to characterize the focusing performance. The imaging results are compared with those of the BF-OCT system. Specifically, in oder to observe the sidelobes more clearly, the aqueous solution of polystyrene microbeads (Cat# SIGMA/LB8-2ML, SIGMA Inc., Dia. 800 nm, ∼0.1 vol.%) was used. Figure 23a shows the real-time tomograph acquired using the BF-OCT system, whereas Fig. 23b presents the image acquired using the DF-OCT system. Results demonstrate that, compared with the BF-OCT system, lateral sidelobes of the image are largely suppressed with the DF-OCT system.

The lateral intensity profiles of microbeads images that are acquired using BF-OCT and DF-OCT setup (Fig. 23c) were also measured to evaluate the sidelobe suppression effect. Experimental results show that the first sidelobe of the DF-OCT system (red solid line) was 3.1 dB smaller than that of the BF-OCT system (Magenta dash-dotted line). Although the lateral resolution was slightly degraded and the amplitudes of higher order sidelobes were elevated in the DF-OCT case (dashed blue line) with respect to the case of BF-OCT (dark dotted line), such effects were secondary since the first sidelobe is the most prominent artifact in OCT images. The measured results agreed well with the numerical simulation results except for the lateral positions of peaks and valleys. Such variances could be caused by the difference between the nominal and actual fiber NA.

4.2 *Imaging Applications with High-Lateral Resolution OCT Systems*

The digital refocusing method based ISAM technique was validated and also applied for real biological scattering tissues, i.e., human breast tissues as illustrated in Fig. 24. By comparing with histological images, it is found that the images by conventional SD-OCT lost most of the features, especially the adipose cell boundaries, which however are fairly distinguishable in ISAM images. However, the significant amount of computation time and the requirement for phase-stable measurement obscure the in vivo implementation of ISAM.

Recently, Ahmad et al. optimized the computation strategies by decomposing 3D problem into two sets of 2D problems so that in vivo real-time implementation of ISAM is achieved [97]. Figure 25 shows an in vivo real-time demonstration of

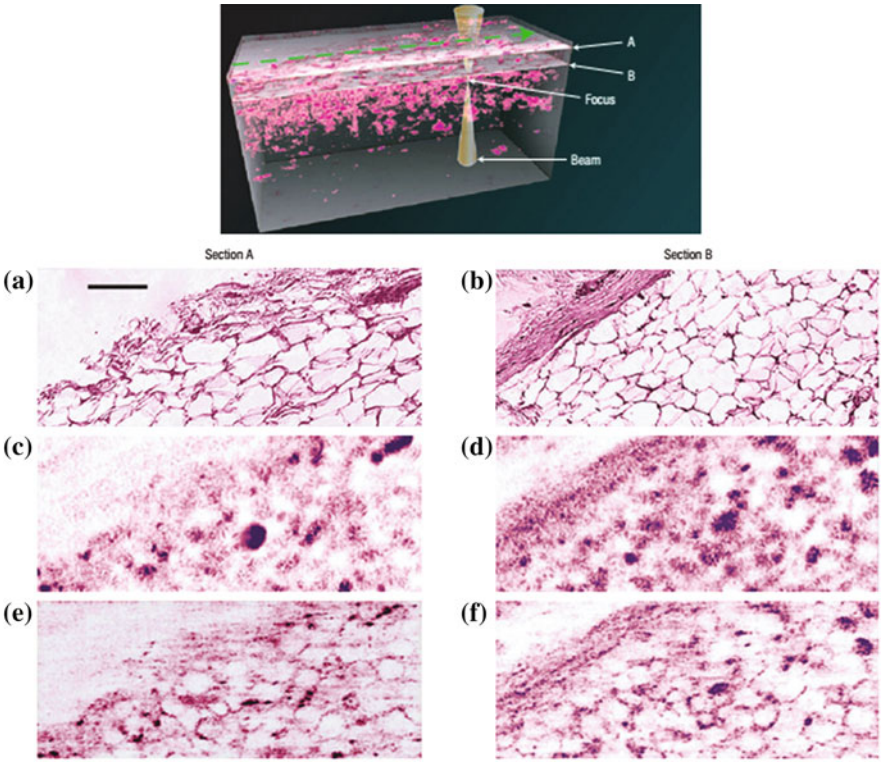

Fig. 24 En-face images of human breast tissues by conventional SD-OCT and ISAM. Two en-face images are chosen from depths A and B which are 591 and 643 μm above the actual focal plane, respectively. **a** and **b** are the histological images; **c** and **d** are the images by conventional SD-OCT; **e** and **f** are the corresponding ISAM images. (Figures are reproduced with permission from [68])

ISAM on human skin. The results demonstrated that ISAM succeeded to extend the depth-of-focus to be 24 times of Rayleigh ranges. It also proved that ISAM improved the SNR in addition to improving the focus of the images from defocused depths (Fig. 25e).

In contrary to the digital refocusing/adaptive optics method, the axicons/microaxicons was usually incorporated in miniaturized OCT endoscopes and needle probes [72, 81–84, 98]. Figure 26a, b depicts the imaging applications of a proposed FD-OCM system with the axicon optics. Schematic of an ultra-miniaturized multi-micro-axicon system for a miniaturized OCT system is depicted in Fig. 26c. With the continuing research efforts, it is believed that axicon optics, especially the microaxicons, will find wide applications in OCT endoscopes and probes.

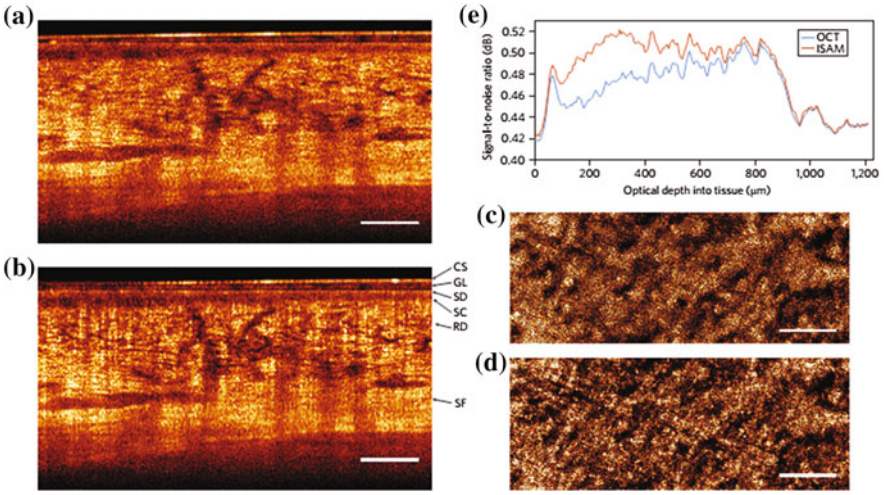

Fig. 25 In vivo real-time demonstration of ISAM on human wrist. **a** and **b** are the two B-scans from conventional SD-OCT and ISAM, respectively. **c** and **d** are two selected en-face images located 520 μm (optical length) away from the skin surface. **e** is the signal-to-noise ratio as a function of optical depth into tissue for both conventional SD-OCT and ISAM. The incident light beam is focused into tissue to be at 1.2 mm (optical length) away from tissue surface. The *scale bar* denotes 500 μm. (Figures are reproduced with permission from [97])

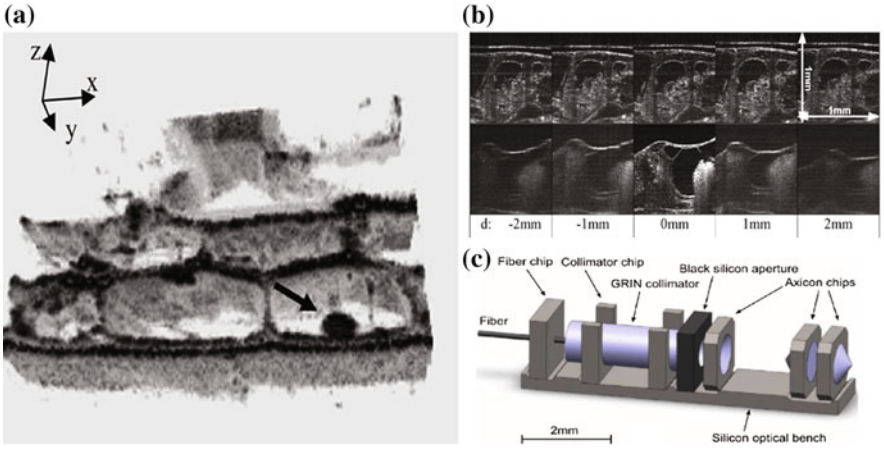

Fig. 26 The imaging application of an axicon based OCT system as well as a miniaturized axicon optical bench. **a** Three dimensional image of onion skin cells captured with xf-FDOCM [72]. **b** SD-OCT images of an African frog tadpole acquired using axicon based OCT system [81]. **c** A schematic design of an ultraminiaturized multi-micro-axicon system for a miniaturized OCT system [98]. (Figures are reproduced with permission from [72, 81])

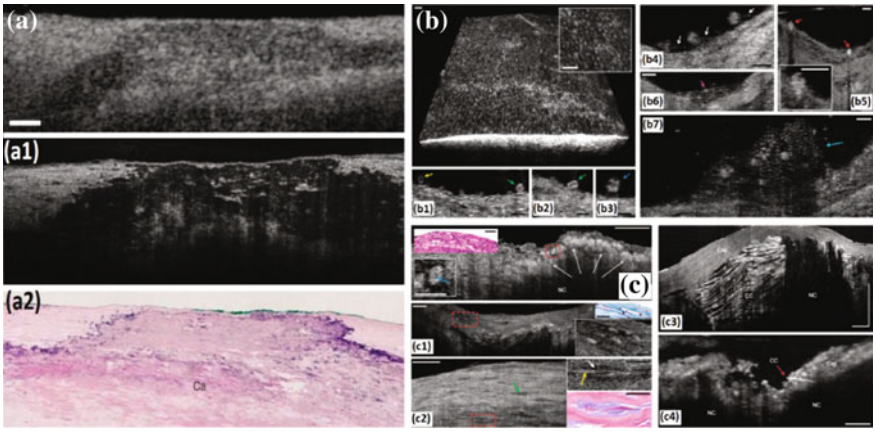

Fig. 27 Subcellular structure of human coronary atherosclerosis acquired with μOCT [92]. **a**–**a2** Images of fibrocalcific human cadaver coronary plaque captured by conventional OCT (**a**), μOCT (**a1**) and histology images (**a2**, H&E). **b**–**b7** μOCT of superficial arterial morphology. **c**–**c4** μOCT images of plaque morphology in human cadaver specimens. (Figures are reproduced with permission from [92])

The μOCT system had been applied for imaging coronary artery disease (CAD) [92], airway epithelia [94], high-speed 3D skin imaging [96] as well as mucociliary transport [95] at subcellular scale. Representative images of human coronary atherosclerosis, airway epithelia and mucociliary transport mechanism acquired by the μOCT system are presented in Figs. 27, 28 and 29, respectively.

5 Recent Developments of High-Resolution OCT Systems

5.1 Ophthalmic Imaging

Ophthalmic imaging is one of the main areas that OCT has found its successful application. Although existing SD-OCT technologies provide a few orders of magnitude higher sensitivity than TD-OCT, the ability of SD-OCT to provide diagnostic information is still limited by its sensitivity, this is because the radiant exposure/irradiance applied to human eyes is restricted to a maximum permissible exposure (MPE) by the international laser safety regulations, e.g., ANSI Z136 in the United States and IEC 60825 [99]. The limited sensitivity in turn limits the OCT penetration depth and/or faster imaging speed.

To address such issues, novel schemes that convert the point source illumination field to line-shaped field have been proposed recently [23, 100–103]. Through utilizing appropriate optic elements, such as cylindrical lens [23], line-field parallel swept source interferometric imaging (LPSI) [100, 101] or dispersive prism/grating

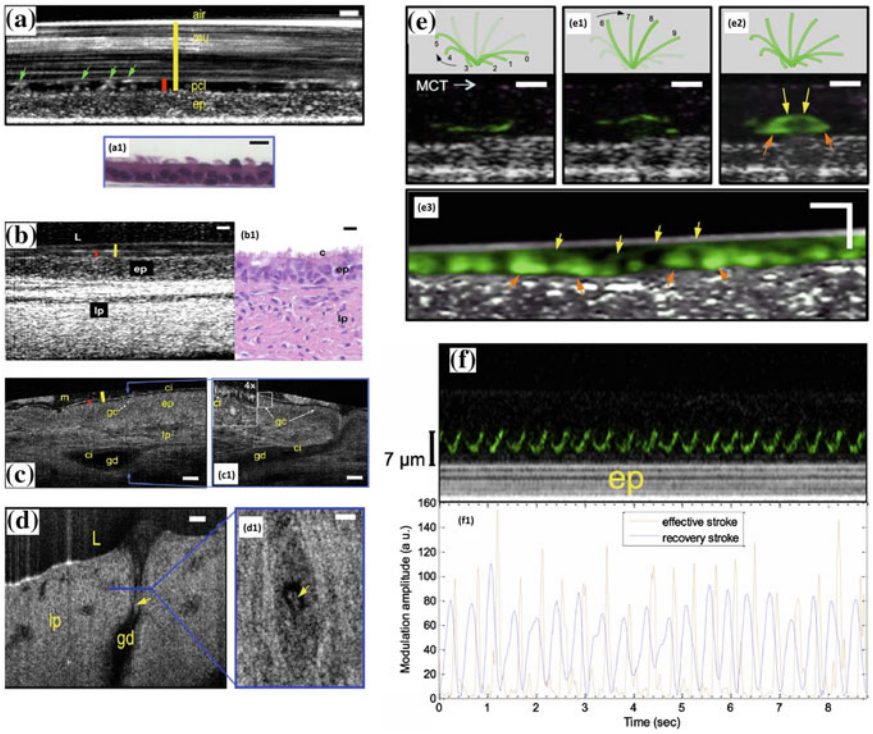

Fig. 28 Quantitative study of airway functional microanatomy using μOCT [94]. **a**–**a1** A time-averaged (2 s) μOCT image of fully differentiated primary human bronchial epithelial cells derived from a normal subject (**a1**) compared to the H&E stained histology of HBE cells. **b**–**b1** μOCT image of functional anatomy of excised swine trachea (**b**) compared to H&E stained histology image (**b1**). **c**–**c1** μOCT images of time averaged (1 s) functional anatomy of human trachea (**c**) and its orthogonal view at the position indicated by the *dashed blue line*. **d**–**d1** Swine mucus (*yellow arrow*) extrusion from a gland duct in lamina propria (**d**) and its three-dimensional reconstructed *en face* view (**d1**). **e**–**e3** μOCT images of ciliary motion pattern in HBE culture and swine trachea. **f**–**f1** Cilia motion pattern in cultured HBE cells. (Figures are reproduced with permission from [94])

[102, 103], to spectrally extend the light source, line-field schemes improve the MPE of the sample also enhance system sensitivity and imaging speed simultaneously. Higher sensitivity in turn improves the penetration depth of the system. Results show that line-field schemes improves the A-line rate significantly up to 823,200 A-lines/s for single frame imaging and 51,500 A-lines/s for continues frame imaging [23], while improves MPE by around 3.1 as compared to the existing point source systems [103]. Such results demonstrate that line-field scheme could be a promising concept for future diagnostic OCT imaging, especially for ophthalmic imaging. In parallel with its advantages in sensitivity and scanning speed improvements, the line-field schemes still suffers from the limited resolution due to the lack of ultra-broadband swept sources.

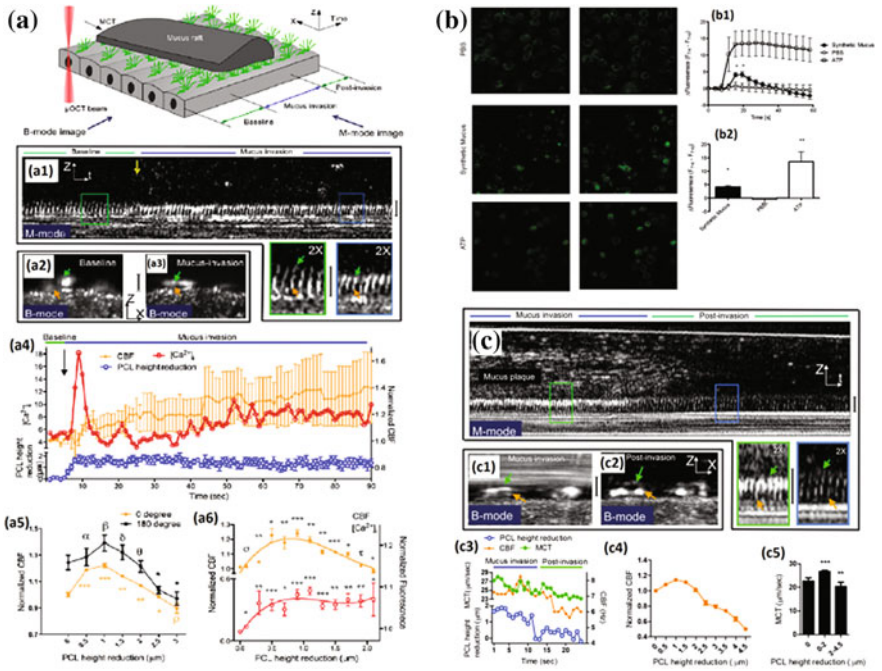

Fig. 29 μOCT for mucociliary transport autoregulatory mechanism study [95]. **a–a5** Periciliary liquid (PCL) height reduction by exogenous mucus load increases $[Ca^{2+}]_i$ and regulates ciliary beat frequency (CBF) in human bronchial epithelial (HBE) cultures. **b–b2** Exogenous mucus stimulates intracellular calcium release in primary HBE cells. **b** Representative images of HBE monolayers loaded with Fluo-4AM to monitor $[Ca^{2+}]$ and treated apically with 50 ml of PBS, synthetic mucus, and ATP (100 mM). **b1–b2** Fluorescent intensity and baseline change over time. **c–c5** PCL height reduction by endogenous mucus plaques regulates CBF in HBE cultures. (Figures are reproduced with permission from [95])

5.2 *Intravascular Imaging*

Intravascular OCT has made significant clinical impact, providing a method of visualizing coronary plaques, optimizing percutaneous coronary intervention, and monitoring treatment results. Among the two incarnations of FD-OCT systems, i.e., SS-OCT and SD-OCT, SS-OCT is the predominant version used in cardiovascular settings, since the type of detectors used tend to be faster and more resistant to motion artifacts. The development of frequency sweeping lasers that cover a wider range of wavelengths is of significant importance to the resolution of SS-OCT, and thus various SS-OCT systems that employ 800 and 1300 nm range laser sources are developed [104].

To confer the advantage of penetration depth offered by the 1300 nm laser without sacrificing the high resolution offered by the 800 nm laser, light sources that emit wavelengths shorter than 1300 nm were developed. Such laser sources

include 800 nm swept laser sources, the 1060 nm OFDI system, as well as some other ultra-broadband OCT sources as reviewed in Sect. 3.1. Various schemes have also been developed to improve the DOF of OCT systems as discussed in Sect. 4.1.

Recently, a new class of OCT systems, termed as Micro-OCT, has been designed to benefit from all these resolution enhancement strategies. Through utilizing a light source centered at 800 nm with extreme breadth from a supercontinuum laser combined with an aperture shape that enhances the axial depth of scan, Micro-OCT achieves 1-μm Axial, 2-μm lateral resolution [92, 104]. Both ex vivo and in vitro imaging using such μOCT have been reported recently [92, 105]. New miniature μOCT endoscopic probes are also being developed, and being validated through experiments in swine airways [104] as well as atherosclerosis and valvular disease imaging [106].

5.3 Gastrointestinal Endoscopy Imaging

Gastrointestinal (GI) endoscopy is another area that OCT system has found its successful clinical applications. Since diseases of the GI tract are commonly diagnosed by endoscopy, and the endoscopy process has certain inefficiencies, such as, subjects are sedated; requiring a specialized setting, equipment, and medical staff to monitor for adverse reactions, etc. Since these efficiencies cause the patient treatment to be cost and time-consuming, hence, a novel, tethered opto-mechanical pill [107] was invented recently. Such tethered capsule employs optical frequency domain (OFDI) imaging technology to captures three-dimensional microscopic images of the digestive organs after it has been swallowed. The capsule probe is connected to a thin, string-like tether that allows the operator to control the position of the capsule in the GI tract, effectuates a circumferential scan of the miniature focusing optics in the pill, and transceives light to and from the capsule. Once swallowed, the luminal organs constrict around the pill and gradually push it down the GI tract under the natural propulsion force of peristalsis. When the capsule probe has reached the distal-most region of interest, it is pulled back using the tether again while imaging. Detailed implementation of such GI imaging system can be found in [107].

The tethered capsule endomicroscopy opens up new possibilities for medical screening and diagnosis of GI tract organs. Specifically, since no sedation or expert operation is required in the imaging process, the tethered capsule endomicroscopy can be conveniently done by a helper or patient him/herself without going to the hospital. Therefore, such tethered capsule endomicroscopy reduces the workload and save both diagnosis time and cost simultaneously.

5.4 Modified Multimodal OCT Schemes

Lack of molecular contrast is one of the major drawbacks of OCT for biological research and some of the clinical applications. There are generally two approaches to compensate for this drawback. Several research groups have implemented various modified OCT schemes that have the capability to detect molecular contrast agents or contrast agents that can potentially bind to a specific chemical or protein. A hybrid optical imaging approach that can combine OCT's ability to perform high-resolution and excellent penetration depth imaging with fluorescence contrast microscopy's ability to elicit molecular contrast from the sample can dramatically enhance the capability of clinicians and biomedical researchers to track biochemical distribution and changes within tissue samples in question.

Pump-probe MCOCT [108] was the first reported approach for performing molecular contrast (enhanced) OCT (MCOCT) imaging. With such scheme, an optical excitation field changes the absorption cross-section of the dye at the OCT probe wavelength by shelving the molecules into a relatively long-lived triplet state. The major challenge with this technique lies in creating a sufficiently fast OCT imaging system to acquire the OCT signal with the dye molecules in the short transition duration in their transition state. To address such issues, some other class of MCOCT, such as pump-suppression MCOCT, spectroscopic OCT, nonlinear interaction based OCT and scattering based MCOCT, etc., have also been developed.

Dual-mode microscopy is a hybrid optical imaging approach that can combine OCT's ability to perform high-resolution and high penetration depth imaging with fluorescence contrast microscopy's ability to elicit molecular contrast from the sample. A dedicated dual-mode microscopy with combined molecular and morphologic contrast machanism can dramatically enhance the clinicians'/biomedical-researchers' capability to track biochemical distribution and changes within tissue. A number of dual-mode microscopy based schemes have been demonstrated and been applied to in vivo imaging for different tissues in recent years [109–111].

6 Conclusions

In the past years, continuous efforts have been devoted towards developing high-resolution systems for cellular and subcellular imaging in OCT community. The main objective of such efforts is for in vivo diagnostics with an accuracy that is comparable to the histopathology. Apparently, cellular and subcellular imaging requires improvement of both lateral and axial resolutions. This chapter gives a review of the developments of SD-OCT systems with high axial- or/and lateral-resolution. For axial resolution enhancement, various broadband bandwidth light sources have been developed. As for lateral resolution, the conventional

way using large NA objective beam improves the lateral resolution but with the price of a reduced depth-of-focus. Consequently, extending DOF has turned out to be a key part of the research on improving lateral resolution. The various DOF extension techniques, including adaptive optics/digital-refocusing, axicon optics and phase/amplitude apodization, are reviewed in this chapter. In addition, the applications of high resolution OCT technologies for different tissue organ systems have also been reviewed.

In the future, the advancements in high-resolution and long DOF OCT technologies will effectively expand the applications of OCT system in clinics as a screening and/or diagnostic tool and improve its clinic values. By far, the most successful translation of OCT into clinic routine is ophthalmic imaging, especially for retinal disease detection. This is because OCT imaging has fairly good axial resolution (<10 μm) and imaging depth up to 2–3 mm, which nicely meet the requirement for examining the layer structure changes associated with eye diseases. For similar reasons, OCT has also found a good application in intravascular imaging. However, for OCT to be successfully adopted in other translational clinical applications, such as stomach, esophagus, colon and lung, ultra-high resolution is highly desired to provide the insights of cellular and subcellular changes at tissue level. Currently, clinical research work on correlating OCT imaging with histopathological imaging has been ongoing. It is believed that high-resolution OCT imaging should be able to significantly enhance the correlation. Besides its potential clinic utilities, high resolution can further help extend OCT's application to research on disease mechanism, which is very critical for developing disease prevention strategies.

In addition to the ultra-high-resolution requirement, some other key issues that determine the performances of an OCT system also need to be addressed. The first one is DOF extension problem. As discussed, although various schemes have been proposed to extend the DOF of an OCT system, yet all these schemes are associated with a serious issue of sidelobes. Such sidelobes, if not managed appropriately, will introduce artifacts to OCT images and thus degrade the effective resolution of the OCT system. The issue of insufficient DOF associated with high lateral resolution OCT technologies will continue to be the major technical obstacle that prevents OCT systems from wide deployment, despite of the multiple DOF extension attempts. Technologies which can extend DOF without significantly sacrificing the imaging sensitivity are highly desirable for clinically viable high lateral resolution OCT devices.

Imaging speed as well as the inherent speckle noise is another problem that needs to be addressed for the clinical application of OCT systems. While speed limits the practical OCT imaging performance and requires relatively long time to acquire dense 3D OCT data sets, speckle noise limits the contrast and SNR of OCT images, making the interpretation of architectural morphologic features for clinical diagnosis difficult. By far, extensive attentions have been paid to such issues and various schemes have been proposed. Among such efforts, SS-OCT systems achieve higher imaging speed as compared to SD-OCT, yet they still suffer from the limited FWHM width of the laser source, and thereby, the system resolutions are

lower. Similarly, even though various techniques, including spatial compounding and digital signal processing algorithms, have been introduced to reduce speckle noise, much more efforts are still needed for the future developments of OCT systems.

OCT is a rapidly evolving technique. Although it still has various limitations in resolutions, imaging speed, sensitivity and penetration depth, etc., it is believed that OCT would find wider application areas in both clinical diagnosis and health care systems in the future, due to rapid advancements of optic technologies. Specifically, as one of the main technologies for OCT DOF extension, digital refocusing is attracting more and more research interests, and could be a key technology for both resolutions and DOF enhancement with acceptable system complexity. The development of broadband swept light sources is another key technology for the development of high-speed ultra-high resolution OCT systems. Moreover, the miniature probe design together with the development of personal data cloud and high-speed huge data processing units offer great potential for OCT to be applied in both cosmetology and pathology. Further advances of OCT technology will bring us to cellular or subcellular level imaging, and thus enable us to determine with confidence what therapeutic strategies are most effective at mitigating risk, and how individual patients would respond to their treatment in the future.

Acknowledgments Jianhua Mo is supported in part by Soochow University, China (Startup grant: Jianhua Mo) and Natural Science Foundation of Jiangsu Province (SBK2014043010). Linbo Liu is supported in part by the Nanyang Technological University (Startup grant: Linbo Liu), National Research Foundation Singapore (NRF2013NRF-POC001-021), National Medical Research Council Singapore (NMRC/CBRG/0036/2013), Ministry of Education Singapore (MOE2013-T2-2-107).

References

1. D. Huang, E.A. Swanson, C.P. Lin, J.S. Schuman, W.G. Stinson, W. Chang, M.R. Hee, T. Flotte, K. Gregory, C.A. Puliafito, J.G. Fujimoto, Optical coherence tomography. Science **254**, 1178–1181 (1991)
2. W. Drexler, J.G. Fujimoto, *Optical Coherence Tomography: Technology and Applications* (Springer, 2008)
3. A.F. Fercher, C.K. Hitzenberger, G. Kamp, S.Y. El-Zaiat, Measurement of intraocular distances by backscattering spectral interferometry. Opt. Commun. **117**, 43–48 (1995)
4. T. Klein, W. Wieser, C.M. Eigenwillig, B.R. Biedermann, R. Huber, Megahertz OCT for ultrawide-field retinal imaging with a 1050 nm Fourier domain mode-locked laser. Opt. Express **19**, 3044–3062 (2011)
5. Y. Hori, Y. Yasuno, S. Sakai, M. Matsumoto, T. Sugawara, V. Madjarova, M. Yamanari, S. Makita, T. Yasui, T. Araki, Automatic characterization and segmentation of human skin using three-dimensional optical coherence tomography. Opt. Express **14**, 1862–1877 (2006)
6. S.A. Boppart, B.E. Bouma, C. Pitris, J.F. Southern, M.E. Brezinski, J.G. Fujimoto, In vivo cellular optical coherence tomography imaging. Nat. Med. **4**, 861–865 (1998)
7. E.J. Fernandez, B. Hermann, B. Povazay, A. Unterhuber, H. Sattmann, B. Hofer, P.K. Ahnelt, W. Drexler, Ultrahigh resolution optical coherence tomography and pancorrection for cellular imaging of the living human retina. Opt. Express **16**, 11083–11094 (2008)

8. M. Choma, M. Sarunic, C. Yang, J. Izatt, Sensitivity advantage of swept source and Fourier domain optical coherence tomography. Opt. Express **11**, 2183–2189 (2003)
9. G. Hausler, M.W. Lindner, "Coherence Radar" and "Spectral Radar"—New tools for dermatological diagnosis. J. Biomed. Opt. **3**, 21–31 (1998)
10. E.A. Swanson, D. Huang, C. Lin, C. Puliafito, M. Hee, J. Fujimoto, High-speed optical coherence domain reflectometry. Opt. Lett. **17**, 151–153 (1992)
11. A.F. Fercher, W. Drexler, C.K. Hitzenberger, T. Lasser, Optical coherence tomography-principles and applications. Rep. Prog. Phys. **66**, 239 (2003)
12. M.E. van Velthoven, D.J. Faber, F.D. Verbraak, T.G. van Leeuwen, M.D. de Smet, Recent developments in optical coherence tomography for imaging the retina. Progr. Retinal Eye Res. **26**, 57–77 (2007)
13. M.R. Hee, J.A. Izatt, E.A. Swanson, D. Huang, J.S. Schuman, C.P. Lin, C.A. Puliafito, J.G. Fujimoto, Optical coherence tomography of the human retina. Arch. Ophthalmol. **113**, 325–332 (1995)
14. M.E. van Velthoven, F.D. Verbraak, L.A. Yannuzzi, R.B. Rosen, A.G. Podoleanu, M.D. De Smet, Imaging the retina by en face optical coherence tomography. Retina **26**, 129–136 (2006)
15. W. Drexler, Ultrahigh-resolution optical coherence tomography. J. Biomed. Opt. **9**, 47–74 (2004)
16. J.F. de Boer, B. Cense, B.H. Park, M.C. Pierce, G.J. Tearney, B.E. Bouma, Improved signal-to-noise ratio in spectral-domain compared with time-domain optical coherence tomography. Opt. Lett. **28**, 2067–2069 (2003)
17. M. Wojtkowski, T. Bajraszewski, P. Targowski, A. Kowalczyk, Real-time in vivo imaging by high-speed spectral optical coherence tomography. Opt. Lett. **28**, 1745–1747 (2003)
18. N. Nassif, B. Cense, B. Hyle Park, S.H. Yun, T.C. Chen, B.E. Bouma, G.J. Tearney, JFd Boer, In vivo human retinal imaging by ultrahigh-speed spectral domain optical coherence tomography. Opt. Lett. **29**, 480–482 (2004)
19. N. Nassif, B. Cense, B. Park, M. Pierce, S. Yun, B. Bouma, G. Tearney, T. Chen, J. de Boer, In vivo high-resolution video-rate spectral-domain optical coherence tomography of the human retina and optic nerve. Opt. Express **12**, 367–376 (2004)
20. E. Götzinger, M. Pircher, C.K. Hitzenberger, High speed spectral domain polarization sensitive optical coherence tomography of the human retina. Opt. Express **13**, 10217–10229 (2005)
21. B. White, M. Pierce, N. Nassif, B. Cense, B. Park, G. Tearney, B. Bouma, T. Chen, J. de Boer, In vivo dynamic human retinal blood flow imaging using ultra-high-speed spectral domain optical coherence tomography. Opt. Express **11**, 3490–3497 (2003)
22. M. Wojtkowski, R. Leitgeb, A. Kowalczyk, A.F. Fercher, T. Bajraszewski, In vivo human retinal imaging by Fourier domain optical coherence tomography. J. Biomed. Opt. **7**, 457–463 (2002)
23. Y. Nakamura, S. Makita, M. Yamanari, M. Itoh, T. Yatagai, Y. Yasuno, High-speed three-dimensional human retinal imaging by line-field spectral domain optical coherence tomography. Opt. Express **15**, 7103–7116 (2007)
24. H.-C. Lee, J.J. Liu, Y. Sheikine, A.D. Aguirre, J.L. Connolly, J.G. Fujimoto, Ultrahigh speed spectral-domain optical coherence microscopy. Biomed. Opt. Express **4**, 1236–1254 (2013)
25. M. Zhang, L. Ma, P. Yu, Dual-band Fourier domain optical coherence tomography with depth-related compensations. Biomed. Opt. Express **5**, 167–182 (2014)
26. B. Cense, N. Nassif, T. Chen, M. Pierce, S.-H. Yun, B. Park, B. Bouma, G. Tearney, J. de Boer, Ultrahigh-resolution high-speed retinal imaging using spectral-domain optical coherence tomography. Opt. Express **12**, 2435–2447 (2004)
27. M. Wojtkowski, V.J. Srinivasan, T.H. Ko, J.G. Fujimoto, A. Kowalczyk, J.S. Duker, Ultrahigh-resolution, high-speed, Fourier domain optical coherence tomography and methods for dispersion compensation. Opt. Express **12**, 2404–2422 (2004)

28. R. Leitgeb, W. Drexler, A. Unterhuber, B. Hermann, T. Bajraszewski, T. Le, A. Stingl, A. Fercher, Ultrahigh resolution Fourier domain optical coherence tomography. Opt. Express **12**, 2156–2165 (2004)
29. J. Schmitt, A. Knüttel, Model of optical coherence tomography of heterogeneous tissue. JOSA A **14**, 1231–1242 (1997)
30. S. Yun, G. Tearney, J. de Boer, N. Iftimia, B. Bouma, High-speed optical frequency-domain imaging. Opt. Express **11**, 2953–2963 (2003)
31. S.H. Yun, G.J. Tearney, B.J. Vakoc, M. Shishkov, W.Y. Oh, A.E. Desjardins, M.J. Suter, R. C. Chan, J.A. Evans, I.K. Jang, N.S. Nishioka, J.F. de Boer, B.E. Bouma, Comprehensive volumetric optical microscopy in vivo. Nat. Med. **12**, 1429–1433 (2006)
32. M. Gora, K. Karnowski, M. Szkulmowski, B.J. Kaluzny, R. Huber, A. Kowalczyk, M. Wojtkowski, Ultra high-speed swept source OCT imaging of the anterior segment of human eye at 200 kHz with adjustable imaging range. Opt. Express **17**, 14880–14894 (2009)
33. E. Braunwald, E.M. Antman, J.W. Beasley, R.M. Califf, M.D. Cheitlin, J.S. Hochman, R.H. Jones, D. Kereiakes, J. Kupersmith, T.N. Levin, C.J. Pepine, J.W. Schaeffer, E.E. Smith 3rd, D.E. Steward, P. Theroux, R.J. Gibbons, J.S. Alpert, D.P. Faxon, V. Fuster, G. Gregoratos, L.F. Hiratzka, A.K. Jacobs, S.C. Smith Jr, ACC/AHA guideline update for the management of patients with unstable angina and non-ST-segment elevation myocardial infarction–2002: summary article: a report of the American College of Cardiology/American Heart Association Task Force on Practice Guidelines (Committee on the Management of Patients With Unstable Angina). Circulation **106**, 1893–1900 (2002)
34. R. Huber, M. Wojtkowski, K. Taira, J. Fujimoto, K. Hsu, Amplified, frequency swept lasers for frequency domain reflectometry and OCT imaging: design and scaling principles. Opt. Express **13**, 3513–3528 (2005)
35. R. Huber, M. Wojtkowski, J.G. Fujimoto, J. Jiang, A. Cable, Three-dimensional and C-mode OCT imaging with a compact, frequency swept laser source at 1300 nm. Opt. Express **13**, 10523–10538 (2005)
36. R. Huber, M. Wojtkowski, J.G. Fujimoto, Fourier domain mode locking (FDML): a new laser operating regime and applications for optical coherence tomography. Opt. Express **14**, 3225–3237 (2006)
37. M.A. Choma, K. Hsu, J.A. Izatt, Swept source optical coherence tomography using an all-fiber 1300-nm ring laser source. J. Biomed. Opt. **10**, 044009-044009-044006 (2005)
38. S. Yun, G. Tearney, B. Bouma, B. Park, J. de Boer, High-speed spectral-domain optical coherence tomography at 1.3 μm wavelength. Opt. Express **11**, 3598–3604 (2003)
39. L. Pantanowitz, P.L. Hsiung, T.H. Ko, K. Schneider, P.R. Herz, J.G. Fujimoto, S. Raza, J.L. Connolly, High-resolution imaging of the thyroid gland using optical coherence tomography. Head Neck **26**, 425–434 (2004)
40. P. Herz, Y. Chen, A. Aguirre, J. Fujimoto, H. Mashimo, J. Schmitt, A. Koski, J. Goodnow, C. Petersen, Ultrahigh resolution optical biopsy with endoscopic optical coherence tomography. Opt. Express **12**, 3532–3542 (2004)
41. P.-L. Hsiung, L. Pantanowitz, A.D. Aguirre, Y. Chen, D. Phatak, T.H. Ko, S. Bourquin, S. J. Schnitt, S. Raza, J.L. Connolly, Ultrahigh-resolution and 3-dimensional optical coherence tomography ex vivo imaging of the large and small intestines. Gastrointest. Endosc. **62**, 561–574 (2005)
42. B. Park, M.C. Pierce, B. Cense, S.-H. Yun, M. Mujat, G. Tearney, B. Bouma, J. de Boer, Real-time fiber-based multi-functional spectral-domain optical coherence tomography at 1.3 μm. Opt. Express **13**, 3931–3944 (2005)
43. M.M. Eberle, C.L. Reynolds, J.I. Szu, Y. Wang, A.M. Hansen, M.S. Hsu, M.S. Islam, D.K. Binder, B.H. Park, In vivo detection of cortical optical changes associated with seizure activity with optical coherence tomography. Biomed. Opt. Express **3**, 2700–2706 (2012)
44. Y. Wang, C.M. Oh, M.C. Oliveira, M.S. Islam, A. Ortega, B.H. Park, GPU accelerated real-time multi-functional spectral-domain optical coherence tomography system at 1300 nm. Opt. Express **20**, 14797–14813 (2012)

45. Y. Watanabe, Y. Takahashi, H. Numazawa, Graphics processing unit accelerated intensity-based optical coherence tomography angiography using differential frames with real-time motion correction. J. Biomed. Opt. **19**, 021105–021105 (2014)
46. C.L. Rodriguez, J.I. Szu, M.M. Eberle, Y. Wang, M.S. Hsu, D.K. Binder, B.H. Park, Decreased light attenuation in cerebral cortex during cerebral edema detected using optical coherence tomography. Neurophotonics **1**, 025004–025004 (2014)
47. B. Povazay, K. Bizheva, A. Unterhuber, B. Hermann, H. Sattmann, A.F. Fercher, W. Drexler, A. Apolonski, W.J. Wadsworth, J.C. Knight, P.S.J. Russell, M. Vetterlein, E. Scherzer, Submicrometer axial resolution optical coherence tomography. Opt. Lett. **27**, 1800–1802 (2002)
48. Y. Wang, J. Nelson, Z. Chen, B. Reiser, R. Chuck, R. Windeler, Optimal wavelength for ultrahigh-resolution optical coherence tomography. Opt. Express **11**, 1411–1417 (2003)
49. S. Bourquin, A. Aguirre, I. Hartl, P. Hsiung, T. Ko, J. Fujimoto, T. Birks, W. Wadsworth, U. Bünting, D. Kopf, Ultrahigh resolution real time OCT imaging using a compact femtosecond Nd: glass laser and nonlinear fiber. Opt. Express **11**, 3290–3297 (2003)
50. B. Potsaid, B. Baumann, D. Huang, S. Barry, A.E. Cable, J.S. Schuman, J.S. Duker, J.G. Fujimoto, Ultrahigh speed 1050 nm swept source/Fourier domain OCT retinal and anterior segment imaging at 100,000 to 400,000 axial scans per second. Opt. Express **18**, 20029–20048 (2010)
51. I. Grulkowski, J.J. Liu, B. Potsaid, V. Jayaraman, C.D. Lu, J. Jiang, A.E. Cable, J.S. Duker, J.G. Fujimoto, Retinal, anterior segment and full eye imaging using ultrahigh speed swept source OCT with vertical-cavity surface emitting lasers. Biomed. Opt. Express **3**, 2733–2751 (2012)
52. S. Makita, T. Fabritius, Y. Yasuno, Full-range, high-speed, high-resolution 1-μm spectral-domain optical coherence tomography using BM-scan for volumetric imaging of the human posterior eye. Opt. Express **16**, 8406–8420 (2008)
53. L. An, P. Li, G. Lan, D. Malchow, R.K. Wang, High-resolution 1050 nm spectral domain retinal optical coherence tomography at 120 kHz A-scan rate with 6.1 mm imaging depth. Biomed. Opt. Express **4**, 245–259 (2013)
54. M. Mujat, R. Chan, B. Cense, B. Park, C. Joo, T. Akkin, T. Chen, J. de Boer, Retinal nerve fiber layer thickness map determined from optical coherence tomography images. Opt. Express **13**, 9480–9491 (2005)
55. P.-L. Hsiung, D.R. Phatak, Y. Chen, A.D. Aguirre, J.G. Fujimoto, J.L. Connolly, Benign and malignant lesions in the human breast depicted with ultrahigh resolution and three-dimensional optical coherence tomography 1. Radiology **244**, 865–874 (2007)
56. M. Esmaeelpour, B. Považay, B. Hermann, B. Hofer, V. Kajic, K. Kapoor, N.J. Sheen, R.V. North, W. Drexler, Three-dimensional 1060-nm OCT: choroidal thickness maps in normal subjects and improved posterior segment visualization in cataract patients. Invest. Ophthalmol. Vis. Sci. **51**, 5260–5266 (2010)
57. V.J. Srinivasan, T.H. Ko, M. Wojtkowski, M. Carvalho, A. Clermont, S.-E. Bursell, Q.H. Song, J. Lem, J.S. Duker, J.S. Schuman, Noninvasive volumetric imaging and morphometry of the rodent retina with high-speed, ultrahigh-resolution optical coherence tomography. Invest. Ophthalmol. Vis. Sci. **47**, 5522–5528 (2006)
58. W. Drexler, J.G. Fujimoto, State-of-the-art retinal optical coherence tomography. Progr. Retinal Eye Res. **27**, 45–88 (2008)
59. A.G. Podoleanu, R.B. Rosen, Combinations of techniques in imaging the retina with high resolution. Progr. Retinal Eye Res. **27**, 464–499 (2008)
60. M. Ruggeri, H. Wehbe, S. Jiao, G. Gregori, M.E. Jockovich, A. Hackam, Y. Duan, C.A. Puliafito, In vivo three-dimensional high-resolution imaging of rodent retina with spectral-domain optical coherence tomography. Invest. Ophthalmol. Vis. Sci. **48**, 1808–1814 (2007)
61. M. Fleckenstein, P.C. Issa, H.-M. Helb, S. Schmitz-Valckenberg, R.P. Finger, H.P. Scholl, K.U. Loeffler, F.G. Holz, High-resolution spectral domain-OCT imaging in geographic

atrophy associated with age-related macular degeneration. Invest. Ophthalmol. Vis. Sci. **49**, 4137–4144 (2008)
62. M.B. Rüegsegger, D. Geiser, P. Steiner, A. Pica, D.M. Aebersold, J.H. Kowal, Noninvasive referencing of intraocular tumors for external beam radiation therapy using optical coherence tomography: a proof of concept. Med. Phys. **41**, 081704 (2014)
63. K. Bizheva, A. Stingl, M. Mei, H.A. Reitsamer, J.E. Morgan, A. Cowey, R. Holzwarth, T. Le, A. Unterhuber, B. Hermann, Imaging ex vivo and in vitro brain morphology in animal models with ultrahigh resolution optical coherence tomography. J. Biomed. Opt. **9**, 719–724 (2004)
64. K. Bizheva, A. Unterhuber, B. Hermann, B. PovazË, H. Sattmann, A.F. Fercher, W. Drexler, M. Preusser, H. Budka, A. Stingl, Imaging ex vivo healthy and pathological human brain tissue with ultra-high-resolution optical coherence tomography. J. Biomed. Opt. **10**, 011006–0110067 (2005)
65. A.R. Tumlinson, J.K. Barton, B. Povazay, H. Sattman, A. Unterhuber, R.A. Leitgeb, W. Drexler, Endoscope-tip interferometer for ultrahigh resolution frequency domain optical coherence tomography in mouse colon. Opt. Express **14**, 1878–1887 (2006)
66. A.R. Tumlinson, B. Považay, L.P. Hariri, J. McNally, A. Unterhuber, J.K. Barton, B. Hermann, H. Sattmann, W. Drexler, In vivo ultrahigh-resolution optical coherence tomography of mouse colon with an achromatized endoscope. J. Biomed. Opt. **11**, 064003-064003-064008 (2006)
67. A.R. Tumlinson, L.P. Hariri, U. Utzinger, J.K. Barton, Miniature endoscope for simultaneous optical coherence tomography and laser-induced fluorescence measurement. Appl. Opt. **43**, 113–121 (2004)
68. T.S. Ralston, D.L. Marks, P.S. Carney, S.A. Boppart, Interferometric synthetic aperture microscopy. Nat. Phys. **3**, 129–134 (2007)
69. J. Mo, M. de Groot, J.F. de Boer, Focus-extension by depth-encoded synthetic aperture in optical coherence tomography. Opt. Express **21**, 10048–10061 (2013)
70. M. de Groot, C.L. Evans, J.F. de Boer, Self-interference fluorescence microscopy: three dimensional fluorescence imaging without depth scanning. Opt. Express **20**, 15253–15262 (2012)
71. L. Liu, C. Liu, W.C. Howe, C. Sheppard, N. Chen, Binary-phase spatial filter for real-time swept-source optical coherence microscopy. Opt. Lett. **32**, 2375–2377 (2007)
72. R.A. Leitgeb, M. Villiger, A.H. Bachmann, L. Steinmann, T. Lasser, Extended focus depth for Fourier domain optical coherence microscopy. Opt. Lett. **31**, 2450–2452 (2006)
73. Y. Yasuno, J.-I. Sugisaka, Y. Sando, Y. Nakamura, S. Makita, M. Itoh, T. Yatagai, Non-iterative numerical method for laterally super resolving Fourier domain optical coherence tomography. Opt. Express **14**, 1006–1020 (2006)
74. G. Liu, S. Yousefi, Z. Zhi, R.K. Wang, Automatic estimation of point-spread-function for deconvoluting out-of-focus optical coherence tomographic images using information entropy-based approach. Opt. Express **19**, 18135–18148 (2011)
75. T.S. Ralston, D.L. Marks, F. Kamalabadi, S.A. Boppart, Deconvolution methods for mitigation of transverse blurring in optical coherence tomography. IEEE Trans. Image Process. **14**, 1254–1264 (2005)
76. L. Yu, B. Rao, J. Zhang, J. Su, Q. Wang, S. Guo, Z. Chen, Improved lateral resolution in optical coherence tomography by digital focusing using two-dimensional numerical diffraction method. Opt. Express **15**, 7634–7641 (2007)
77. G. Liu, Z. Zhi, R.K. Wang, Digital focusing of OCT images based on scalar diffraction theory and information entropy. Biomed. Opt. Express **3**, 2774–2783 (2012)
78. Z. Jaroszewicz, A. Burvall, A.T. Friberg, Axicon-the most important optical element. Opt. Photonics News **16**, 34–39 (2005)
79. I. Golub, Fresnel axicon. Opt. Lett. **31**, 1890–1892 (2006)
80. Z. Ding, H. Ren, Y. Zhao, J.S. Nelson, Z. Chen, High-resolution optical coherence tomography over a large depth range with an axicon lens. Opt. Lett. **27**, 243–245 (2002)

81. K.-S. Lee, J.P. Rolland, Bessel beam spectral-domain high-resolution optical coherence tomography with micro-optic axicon providing extended focusing range. Opt. Lett. **33**, 1696–1698 (2008)
82. D. Lorenser, C. Christian Singe, A. Curatolo, D.D. Sampson, Energy-efficient low-Fresnel-number Bessel beams and their application in optical coherence tomography. Opt. Lett. **39**, 548–551 (2014)
83. M. Villiger, J. Goulley, M. Friedrich, A. Grapin-Botton, P. Meda, T. Lasser, R.A. Leitgeb, In vivo imaging of murine endocrine islets of Langerhans with extended-focus optical coherence microscopy. Diabetologia **52**, 1599–1607 (2009)
84. C. Blatter, B. Grajciar, C.M. Eigenwillig, W. Wieser, B.R. Biedermann, R. Huber, R.A. Leitgeb, Extended focus high-speed swept source OCT with self-reconstructive illumination. Opt. Express **19**, 12141–12155 (2011)
85. X. Yu, X. Liu, J. Gu, D. Cui, J.L.L. Wu, Depth extension and sidelobe suppression in optical coherence tomography using pupil filters. Opt. Express **22**, 11 (2014)
86. H. Wang, F. Gan, High focal depth with a pure-phase apodizer. Appl. Opt. **40**, 5658–5662 (2001)
87. M. Gu, C. Sheppard, X. Gan, Image formation in a fiber-optical confocal scanning microscope. JOSA A **8**, 1755–1761 (1991)
88. L. Liu, F. Diaz, L. Wang, B. Loiseaux, J.-P. Huignard, C. Sheppard, N. Chen, Superresolution along extended depth of focus with binary-phase filters for the Gaussian beam. JOSA A **25**, 2095–2101 (2008)
89. D. Lorenser, X. Yang, D.D. Sampson, Ultrathin fiber probes with extended depth of focus for optical coherence tomography. Opt. Lett. **37**, 1616–1618 (2012)
90. C.J. Sheppard, S. Mehta, Three-level filter for increased depth of focus and Bessel beam generation. Opt. Express **20**, 27212–27221 (2012)
91. Y. Xu, J. Singh, C.J. Sheppard, N. Chen, Ultra long high resolution beam by multi-zone rotationally symmetrical complex pupil filter. Opt. Express **15**, 6409–6413 (2007)
92. L. Liu, J.A. Gardecki, S.K. Nadkarni, J.D. Toussaint, Y. Yagi, B.E. Bouma, G.J. Tearney, Imaging the subcellular structure of human coronary atherosclerosis using micro-optical coherence tomography. Nat. Med. **17**, 1010–1014 (2011)
93. E. Bousi, S. Timotheou, C. Pitris, Design of pupil filter for extended depth of focus and lateral superresolution in optical coherence tomography, in *SPIE BiOS*, (International Society for Optics and Photonics, 2014), 893435-893435-893437
94. L. Liu, K.K. Chu, G.H. Houser, B.J. Diephuis, Y. Li, E.J. Wilsterman, S. Shastry, G. Dierksen, S.E. Birket, M. Mazur, Method for quantitative study of airway functional microanatomy using micro-optical coherence tomography. PLoS ONE **8**, e54473 (2013)
95. L. Liu, S. Shastry, S. Byan-Parker, G. Houser, K. Chu, S.E. Birket, C.M. Fernandez, J. Gardecki, W. Grizzle, E. Wilsterman, An autoregulatory mechanism governing mucociliary transport is sensitive to mucus load. Am. J. Respir. Cell Mol. biol. (2014)
96. P. Tankam, A.P. Santhanam, K.-S. Lee, J. Won, C. Canavesi, J.P. Rolland, Parallelized multi–graphics processing unit framework for high-speed Gabor-domain optical coherence microscopy. J. Biomed. Opt. **19**, 071410–071410 (2014)
97. A. Ahmad, N.D. Shemonski, S.G. Adie, H.-S. Kim, W.-M.W. Hwu, P.S. Carney, S.A. Boppart, Real-time in vivo computed optical interferometric tomography. Nat. Photonics **7**, 444–448 (2013)
98. N. Weber, D. Spether, A. Seifert, H. Zappe, Highly compact imaging using Bessel beams generated by ultraminiaturized multi-micro-axicon systems. JOSA A **29**, 808–816 (2012)
99. I.E. Commission, IEC 60825-1, *Safety of Laser Products—Part 1*(2001)
100. D.J. Fechtig, T. Schmoll, B. Grajciar, W. Drexler, R.A. Leitgeb, Line-field parallel swept source interferometric imaging at up to 1 MHz. Opt. Lett. **39**, 5333–5336 (2014)
101. D.J. Fechtig, B. Grajciar, T. Schmoll, C. Blatter, R.M. Werkmeister, W. Drexler, R.A. Leitgeb, Line-field parallel swept source MHz OCT for structural and functional retinal imaging. Biomed. Opt. Express **6**, 716–735 (2015)

102. X. Yu, X. Liu, D. Cui, J. Gu, L. Liu, Ultrahigh-resolution optical coherence tomography with enhanced sensitivity and imaging depth using spectrally extended source. Opt. Express **Submitted** (2015)
103. X. Liu, X. Yu, H. Tang, D. Cui, M.R. Beotra, M.J. Girard, D. Sun, J. Gu, L. Liu, Spectrally encoded extended source optical coherence tomography. Opt. Lett. **39**, 6803–6806 (2014)
104. K.K. Chu, G.J. Ughi, L. Liu, G.J. Tearney, Toward clinical μOCT—a review of resolution-enhancing technical advances. Curr. Cardiovasc. Imaging Rep. **7**, 1–8 (2014)
105. M. Kashiwagi, L. Liu, K.K. Chu, C.-H. Sun, A. Tanaka, J.A. Gardecki, G.J. Tearney, Feasibility of the assessment of cholesterol crystals in human macrophages using micro optical coherence tomography. PLoS ONE **9**, e102669 (2014)
106. Y. Nomura, K.K. Chu, J.A. Gardecki, C.-H. Sun, L. Liu, E. Martinez-Martinez, E. Aikawa, G.J. Tearney, Innovations in microscopic imaging of atherosclerosis and valvular disease, in *Cardiovascular Imaging* (Springer, 2015), pp. 251–265
107. M.J. Gora, J.S. Sauk, R.W. Carruth, K.A. Gallagher, M.J. Suter, N.S. Nishioka, L.E. Kava, M. Rosenberg, B.E. Bouma, G.J. Tearney, Tethered capsule endomicroscopy enables less invasive imaging of gastrointestinal tract microstructure. Nat. Med. **19**, 238–240 (2013)
108. Z. Yaqoob, E. McDowell, J. Wu, C. Yang, Pump-probe optical coherence tomography using indocyanine green as a contrast agent, in *Biomedical Optics 2006*, (International Society for Optics and Photonics, 2006), 607904-607904-607908
109. E. Beaurepaire, L. Moreaux, F. Amblard, J. Mertz, Combined scanning optical coherence and two-photon-excited fluorescence microscopy. Opt. Lett. **24**, 969–971 (1999)
110. H. Tu, Y. Zhao, Y. Liu, Y.-Z. Liu, S. Boppart, Noise characterization of broadband fiber Cherenkov radiation as a visible-wavelength source for optical coherence tomography and two-photon fluorescence microscopy. Opt. Express **22**, 20138–20143 (2014)
111. Y. Yoon, W.H. Jang, P. Xiao, B. Kim, T. Wang, Q. Li, J.Y. Lee, E. Chung, K.H. Kim, In vivo wide-field reflectance/fluorescence imaging and polarization-sensitive optical coherence tomography of human oral cavity with a forward-viewing probe. Biomed. Opt. Express **6**, 524–535 (2015)